Chapter 7

Expected Performance

7.1 Simulation of γ and π^0 Detection

7.1.1 BELLE Simulation

The performance of the calorimeter is influenced strongly by the materials in front of the calorimeter. For example, if a γ is converted to an e^+e^- pair by the CDC or ACC wall materials, the γ can not be measured properly by the calorimeter. Fig. 7.1 shows the first interaction point of 100 MeV γ's generated uniformly in 4π and went through the GEANT simulation of the BELLE detector. The electron and positron produced by the interaction will be deflected by the magnetic field and many of them will be lost in the reconstruction. The detection efficiency become lower and the resolution becomes worse. It is important to check the performance of the calorimeter as a part of the whole BELLE detector. Since the whole detector is inside the magnetic field and each component has a complicated shape the simulation is the only possible method of checking.

The BELLE full simulation package is used for this study. This includes the $B^0\bar{B}^0$ and B^+B^- event generator and the GEANT simulator to track the decay and the interaction of produced particles in the detector. The $B^0\bar{B}^0$ and B^+B^- are produced from the Υ(4S) and each B meson decays with the known branching fraction. After the decay, the particles are boosted to the laboratory system and passed to the GEANT simulator. All inner detectors except the endcap ACC are installed in the used version. All the energy deposits of the CsI(Tℓ) crystals are smeared with the electronics noise. The energy deposits in the crystal are combined into an electromagnetic shower using a clustering program developed for the BELLE data analysis, and the energy of the

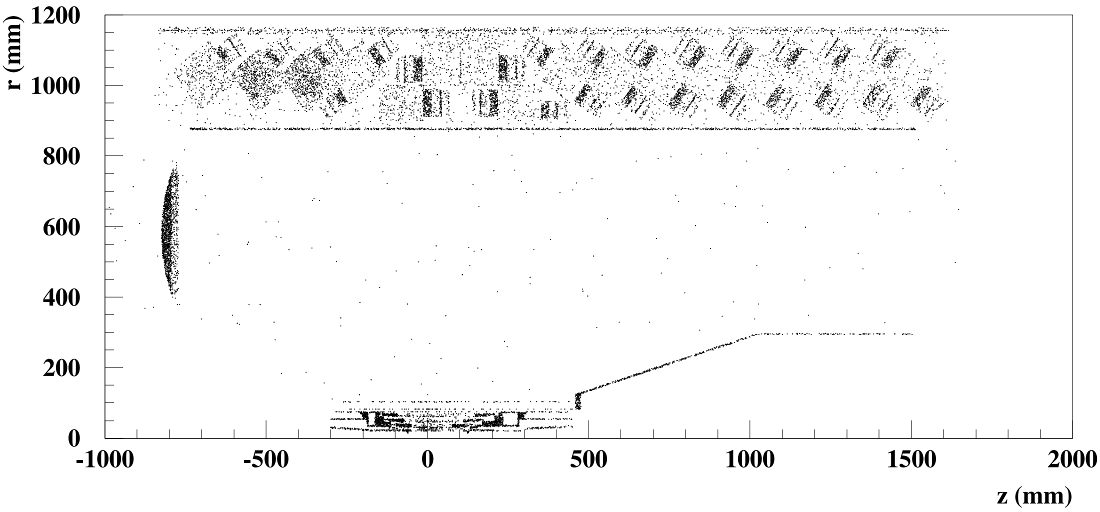

Figure 7.1: First interaction points of 100 MeV γ's generated uniformity in the detector.

shower is determined. The π^0 is reconstructed from any combination of 2 clusters by calculating an invariant mass. The number of generated events are 25k with inner detectors (detector ON) and 30k without inner detectors (detector OFF).

In the following sections, the performance of γ and π^0 detection is discussed from the reconstruction results.

7.1.2 γ Detection

A cluster is formed first by finding a seed counter. The energy of the seed counter should be more than a certain threshold value and 5 MeV for this analysis. When a seed counter is found, the energy of 5 × 5 counters around the seed are summed up and a cluster is formed. The threshold for each counter is 0.5 MeV. If there are two seed counters in the 5 × 5 matrix, two clusters are reconstructed so far as there is at least one counter between two seeds and its energy is lower than any of the seeds. Such a case happens for two γ's from a high momentum π^0 or by accidental overlap of two γ's. After the cluster is formed, the energy deposit is corrected for the shower leakage effect. The cluster position by the center of gravity is corrected by the correction curve.

We selected good γ clusters by applying following 3 cuts;

1. opening angle between generated γ and the reconstructed cluster $\leq 2.5°$.
2. $E_9/E_{25} \geq 0.9$.
3. $\hat{R}_\gamma - 3\sigma^L_{R_\gamma} \leq R_\gamma \leq \hat{R}_\gamma + 3\sigma^H_{R_\gamma}$

The each parameter will be explained later.

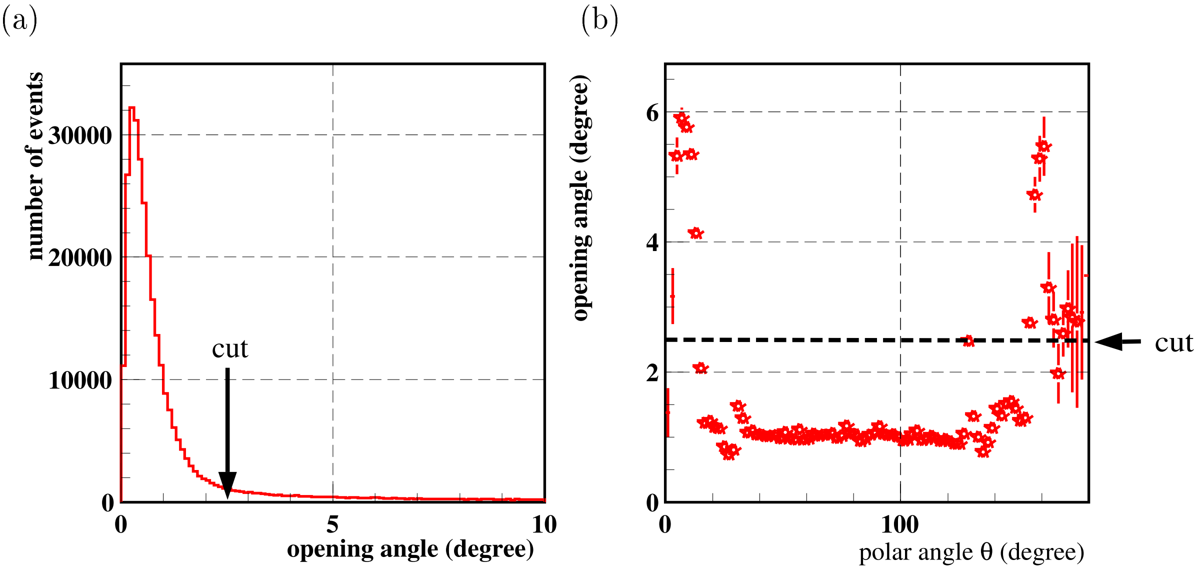

Figure 7.2: (a)Opening angle between CsI cluster and the generated γ and (b) Polar angle dependence of the average opening angle.

The 1st cut was applied to find a matching between the generated γ and the reconstructed cluster. For each generated γ, we calculated the opening angle with any of the clusters and selected the nearest one. If the opening angle is less than 2.5°, the matching is taken. The distribution of the opening angle is shown in Fig. 7.2.

The second cut is applied to check whether the shape of the cluster is consistent with the γ-ray. The γ makes an electromagnetic shower and most of the energy is deposited near the center of the cluster. On the other hand, the shower generated by hadrons tends spread over many clusters. When a γ is converted into an e^+e^- pair before entering the calorimeter, it also tends to produce a 'fat' shower due to the magnetic deflection of e^+e^-. We used the energy deposit of 3 × 3 counters (E_9) and 5 × 5 counters (E_{25}) around the seed to implement this cut. The clusters are rejected if the ratio E_9/E_{25} is less than 0.9. The distribution is shown in Fig. 7.3(a).

For these events after E_9/E_{25} cut, we plotted $R_\gamma \equiv E_\gamma^{REC}/E_\gamma^{GEN}$ where E_γ^{REC} is the energy reconstructed by the cluster program and E_γ^{GEN} is the generated γ energy. The distribution is then fitted by the logarithmic Gaussian and the peak $\hat{R}_\gamma$ and its width $\sigma_{R_\gamma}^L$ for the low energy side and $\sigma_{R_\gamma}^H$ for the high energy side are determined. We selected the events within ± 3 σ as good reconstructed γ's as shown in Fig. 7.3(b).

The results are shown in Fig. 7.4 and Table 7.1 for both cases of inner detector ON and OFF. The efficiency given here is calculated for all the γ's generated in the $B\bar{B}$ decay including the ones which is generated along the beam line and not covered

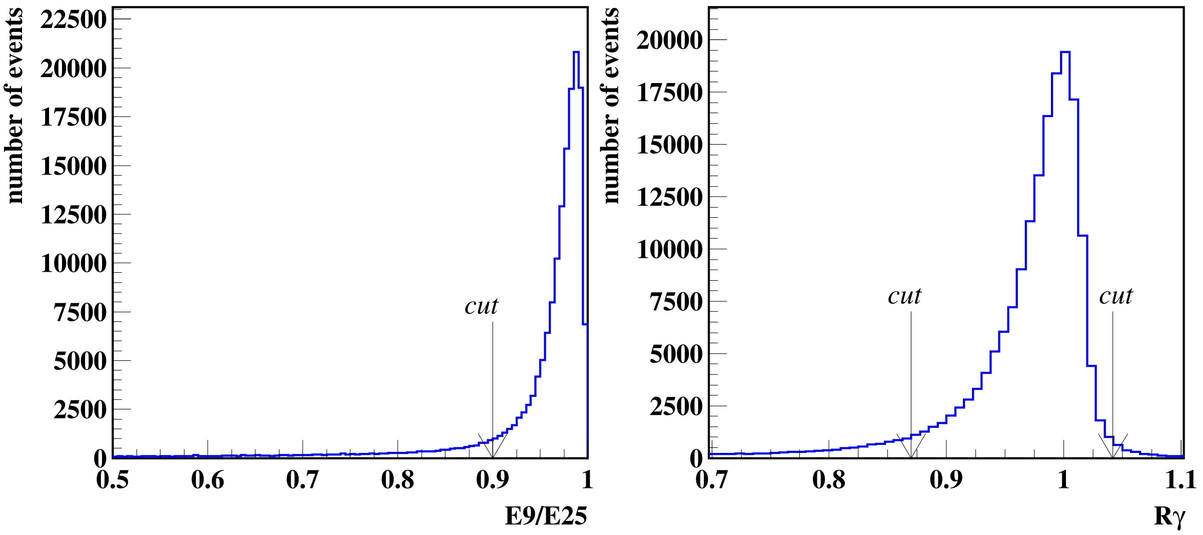

(a) (b)

Figure 7.3: (a)E_9/E_{25} distribution after 'cut 1' (opening angle $\leq 2.5°$), and (b)R_γ distribution after 'cut 2' ($E_9/E_{25} \geq 0.9$).

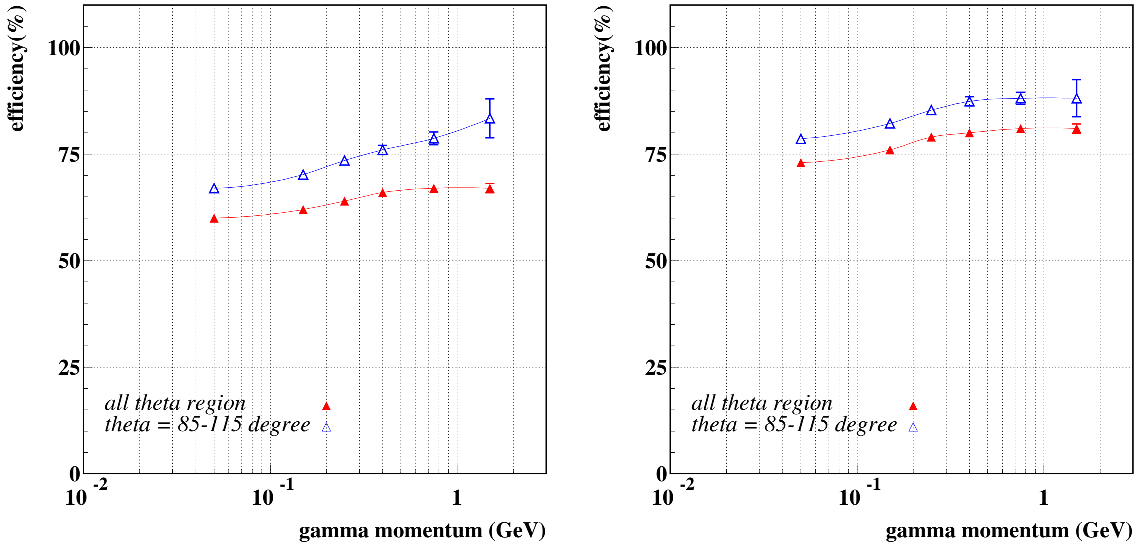

(a) (b)

Figure 7.4: Momentum dependence of γ detection efficiency for (a)inner detector ON and (b)OFF after applying all selection cuts.

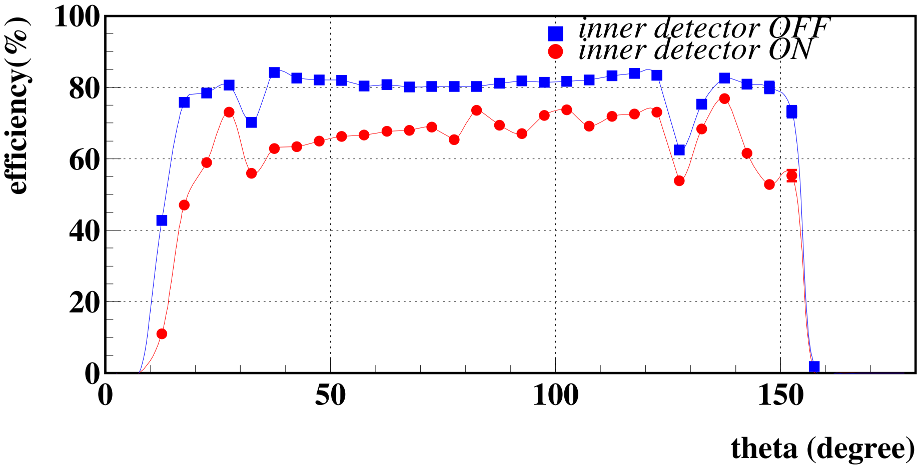

Figure 7.5: Polar angle (θ) dependence of γ detection efficiency.

by the CsI(Tℓ) calorimeter. The γ detection efficiency of BELLE is 60 ~ 65 %, and it depends on the angle and energy of γ's. In the middle of barrel (85° ~ 115°), the efficiency becomes higher than 80 %. Both of them are the results of the detector ON case. The loss of efficiency by the material in front of the calorimeter is about 10 %.

	Inner detector OFF (%)	Inner detector ON (%)
cut 1	93	83
cut 2	85	74
cut 3	76	63

Table 7.1: Cut dependence of the γ detection efficiency for $B\bar{B}$ events. Detector geometrical acceptance is included in the efficiency.

The theta dependence in Fig. 7.5 shows the low efficiency at the gap between barrel and endcap. But the efficiency still stays at more than 50 %.

7.1.3 π^0 Mass Resolution

We selected the clusters originating from the γ by applying the opening angle and E_9/E_{25} cuts described in the previous section. When we analyze the real data, the opening angle cut will be replaced by the CDC track - CsI cluster matching cut. This cut will select only 'neutral' clusters which have no matched charged tracks nearby. For the time being, we proceed for the analysis of π^0 using the γ clusters selected by the opening angle and E_9/E_{25} cuts.

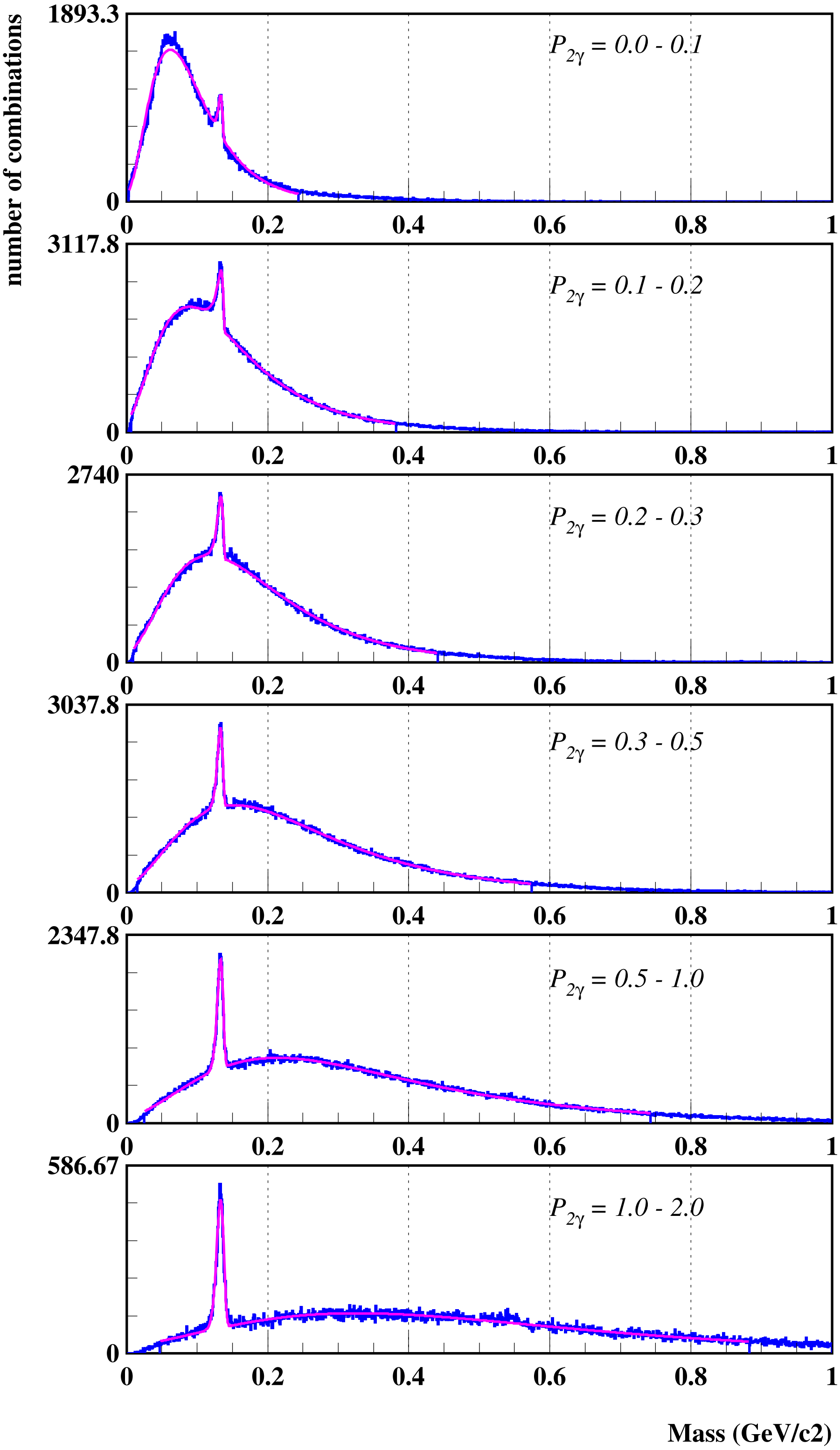

Figure 7.6: Invariant mass $M_{\gamma\gamma}$ distribution of any combination of 2 γ clusters for each momentum region ($0-0.1$, $0.1-0.2$, $0.2-0.3$, $0.3-0.5$, $0.5-1.0$, $1.0-2.0$ GeV), for $B\bar{B}$ generic events. The number of generated events is 25,000.

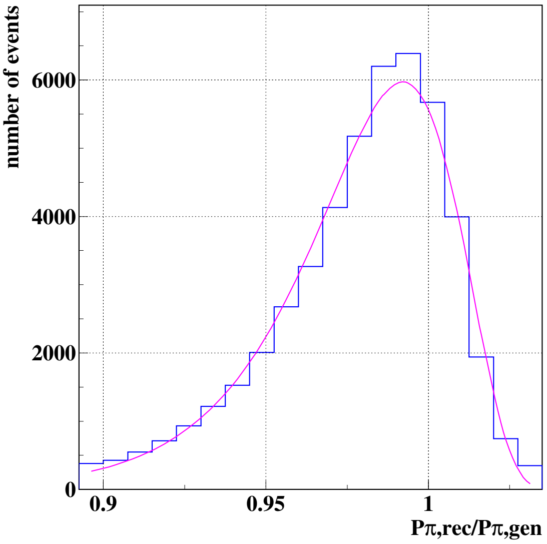

Figure 7.7: π^0 momentum distribution (reconstructed momentum/generated momentum) for all momentum regions with logarithmic Gaussian fit.

We calculated the invariant mass $M_{\gamma\gamma}$ and its associated momentum $P_{\gamma\gamma}$ for any combination of 2 γ clusters in one event. The distribution of $M_{\gamma\gamma}$ is plotted in Fig. 7.6 for each region of $P_{\gamma\gamma}$. The π^0 mass peak around 135 MeV [51] is clearly observed for all momentum regions. The distribution is fitted by Gaussian + logarithmic Gaussian. The normal Gaussian corresponds to the π^0 mass peak and the logarithmic Gaussian explains the combinatorial background. Table. 7.2 summarizes the position of π^0 mass peak M_{π^0} and the mass resolution $\sigma_{M_{\pi^0}}$ for each momentum region. The mass resolution becomes worse at energies above 1 GeV due to the angular resolution of the cluster, but the π^0 peak is distinguishable in all momentum ranges.

7.1.4 Selection of π^0

The π^0 signal is then selected by applying a cut on the invariant mass and its reconstructed momentum with respect to the generated momentum.

- $M_{\pi^0} - 3\sigma_{M_{\pi^0}} \leq M_{\gamma\gamma} \leq M_{\pi^0} + 3\sigma_{M_{\pi^0}}$
- $\hat{R}_{\pi^0} - 3\sigma^L_{R_{\pi^0}} \leq R_{\pi^0} \leq \hat{R}_{\pi^0} + 3\sigma^H_{R_{\pi^0}}$

where $R_{\pi^0} \equiv P^{REC}_{\pi^0}/P^{GEN}_{\pi^0}$, $P^{REC}_{\pi^0}$ and $P^{GEN}_{\pi^0}$ are reconstructed and generated π^0 momentum,respectively. The second cut on R_{π^0} is to check whether the generated momentum is properly restored by the reconstruction program. For events passing

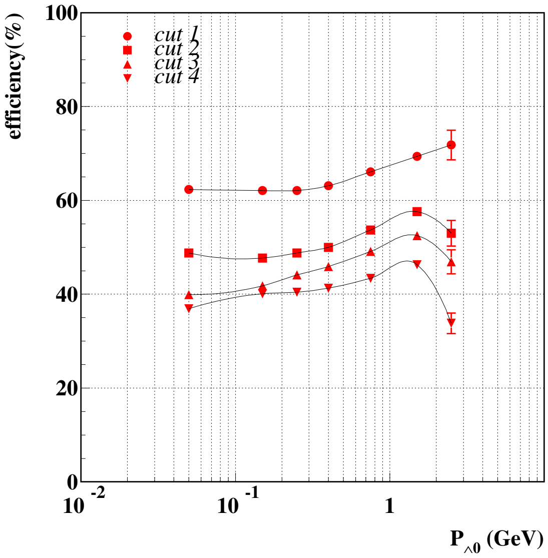

Figure 7.8: Momentum dependence of π^0 detection efficiency after each cut. (cut1 : opening angle between generated γ and the reconstructed cluster $\leq 2.5°$ for 2 γ's, cut2 : $E_9/E_{25} \geq 0.9$. for 2 γ's, cut3 : $M_{\pi^0} - 3\sigma_{M_{\pi^0}} \leq M_{\gamma\gamma} \leq M_{\pi^0} + 3\sigma_{M_{\pi^0}}$, cut4 : $\hat{R}_{\pi^0} - 3\sigma^L_{R_{\pi^0}} \leq R_{\pi^0} \leq \hat{R}_{\pi^0} + 3\sigma^H_{R_{\pi^0}}$.)

the $M_{\gamma\gamma}$ cut, we looked into the MC generator information and selected the genuine π^0 events. The distribution of R_{π^0} for such good π^0's is shown in Fig. 7.7. The distribution is fitted by the logarithmic Gaussian and the momentum resolution is determined.

The values of R_{π^0} and the resolution are summarized in Table. 7.2 for both cases of inner detector ON and OFF. The average resolution of the π^0 momentum reconstruction is 2.3 % and it varies from 3.6 % below 100 MeV to 1.9 % above 1 GeV.

7.1.5 π^0 Detection Efficiency

The π^0 particle is identified if a particular combination of two gamma clusters satisfied all the cuts. The number of such events for each momentum region is counted and is divided by the total number of π^0's generated at all the angles in the same momentum region. This gives the π^0 detection efficiency. The results is given in Fig. 7.8 where the reduction after each cut is demonstrated as a function of the momentum and summarized in Table. 7.2. The detection efficiency improves towards higher momentum. But it starts decreasing above 1 GeV because the angle between two γ's becomes too close at high momentum. If the separation of two γ's becomes less than 1 counter size, the detection of π^0 is difficult. In this case, we need the special treatments to separate

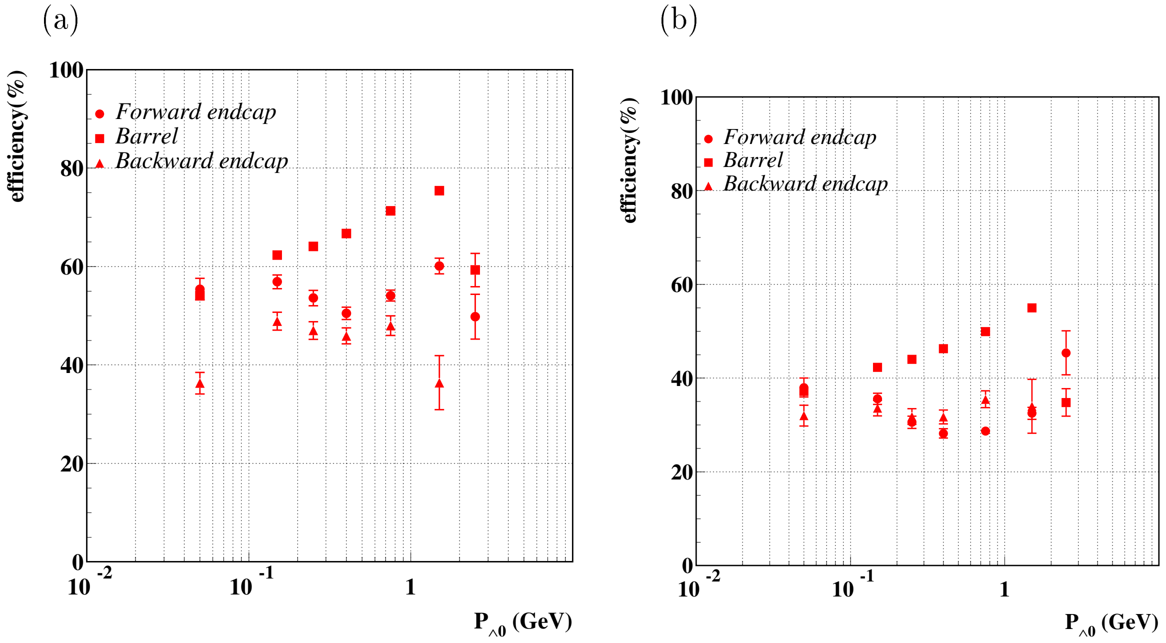

Figure 7.9: Momentum dependence of π^0 detection efficiency for (a)inner detector OFF and (b)ON. The efficiency is shown for Barrel and Forward, Backward endcap calorimeter separately.

them into two γ's.

The π^0 detection efficiency depends on the θ region. Fig. 7.9 shows the efficiency for the barrel and the endcap calorimeter separately.

7.1.6 S/N Ratio

As shown in Fig. 7.6, the reconstructed π^0's include many fake candidates from the combinatorial background. The signal to noise ratio (S/N) is estimated by the following procedure.

For all the combinations of 2 gamma clusters passing the 3 cuts, we looked into the generator information and distinguished the genuine pair of γ's coming from the π^0 (= S) and the fake pairs coming from the combinatorial background (= N). The S/N ratio for each momentum region is listed in Table. 7.2. The S/N ratio becomes better at high momentum and for the case of inner detector OFF as expected.

7.1.7 Summary

Table. 7.2 lists the summary of the π^0 detection performance. The BELLE electromagnetic calorimeter has 65 % efficiency for the γ of a energy 200 MeV and 40 % efficiency for the $\pi^0$of momentum of 100 MeV. These efficiencies are estimated for γ's and π^0's in the $B^0\bar{B}^0$ and B^+B^- decays. These efficiencies might be improved in some amounts by updating the current clustering programs. Those efforts are in progress now.

(a)

π^0 momentum P_{π^0} (GeV)	π^0 mass M_{π^0} (MeV)	π^0 mass resolution $\sigma_{M_{\pi^0}}$ (MeV)	R_{π^0}	momentum resolution $\sigma_{R_{\pi^0}}/R_{\pi^0}(\%)$	S/N	detection efficiency $\eta(\%)$
all	133.1	4.0	0.99	2.3	0.44	41.6 ± 0.2
0.0-0.1	133.5	2.9	0.99	3.6	0.22	36.9 ± 0.6
0.1-0.2	133.9	4.7	0.99	2.8	0.21	40.1 ± 0.4
0.2-0.3	133.6	4.1	0.99	2.4	0.41	40.4 ± 0.5
0.3-0.5	133.0	3.8	0.99	2.2	0.93	41.3 ± 0.4
0.5-1.0	133.1	4.1	0.99	2.0	2.16	43.4 ± 0.4
1.0-2.0	133.2	5.1	0.99	1.9	2.63	46.3 ± 0.7

(b)

π^0 momentum P_{π^0} (GeV)	π^0 mass M_{π^0} (MeV)	π^0 mass resolution $\sigma_{M_{\pi^0}}$ (MeV)	R_{π^0}	momentum resolution $\sigma_{R_{\pi^0}}/R_{\pi^0}(\%)$	S/N	detection efficiency $\eta(\%)$
all	133.2	4.0	0.99	2.3	0.54	53.9 ± 0.7
0.0-0.1	133.4	3.3	0.99	3.3	0.34	59.9 ± 0.5
0.1-0.2	133.7	3.7	0.99	2.5	0.32	60.2 ± 0.5
0.2-0.3	133.3	3.9	0.99	2.3	0.58	61.3 ± 0.4
0.3-0.5	133.1	3.8	0.99	2.2	1.24	64.3 ± 0.4
0.5-1.0	133.3	4.2	0.99	2.0	2.88	67.2 ± 0.7
1.0-2.0	133.1	5.1	0.99	1.9	3.95	60.0 ± 2.6

Table 7.2: π^0 detection performance of BELLE CsI(Tℓ) calorimeter for (a) Inner detector ON and (b) OFF.

Chapter 8

Conclusion

Our purpose in the B-factory is to know the mechanism of the CP violation by using B meson decays. We constructed the BELLE detector for that purpose. The electromagnetic calorimeter is the important part of BELLE to detect electrons and photons.

In order to build a calorimeter with good performance, we chose the CsI(Tℓ) crystal and 8736 counters are produced in total. We got all the counters stable and uniform in performance. The size of the crystals are manufactured within $+0.2$ -0.5 mm of the design values. The light output and the uniformity of all the counters were measured by cosmic ray muons. The average light output is 4969 electron-hole pairs/MeV and the average non-uniformity is 9 %. The light output was stable within ± 1 % over 6 months.

We carried out a beam test by using the photon beam at the Budker Institute of Nuclear Physics (BINP), Russia in autumn, 1997 to confirm the performance of our electromagnetic calorimeter and to establish the analysis and calibration methods of the calorimeter data. The beam test was successfully completed.

The electronics noise which is most effective for the energy resolution is kept minimum during the beam test. As a result, we obtained the energy resolution as follows;

$$\frac{\sigma}{E} = \frac{0.066(\%)}{E} \oplus \frac{0.81(\%)}{E^{1/4}} \oplus 1.34(\%), \quad E \text{ in GeV.} \tag{8.1}$$

It is 4 % at 20 MeV and 1.5 % at 5.4 GeV. To our knowledge, this result is better than any other similar detectors constructed, or being constructed all over the world. Most of the results have good agreement with Monte Carlo simulations and it means that we proved the GEANT simulation well reproduces the electromagnetic shower in the CsI(Tℓ). A properly tuned GEANT simulation will be a useful tool to understand the BELLE experimental data.

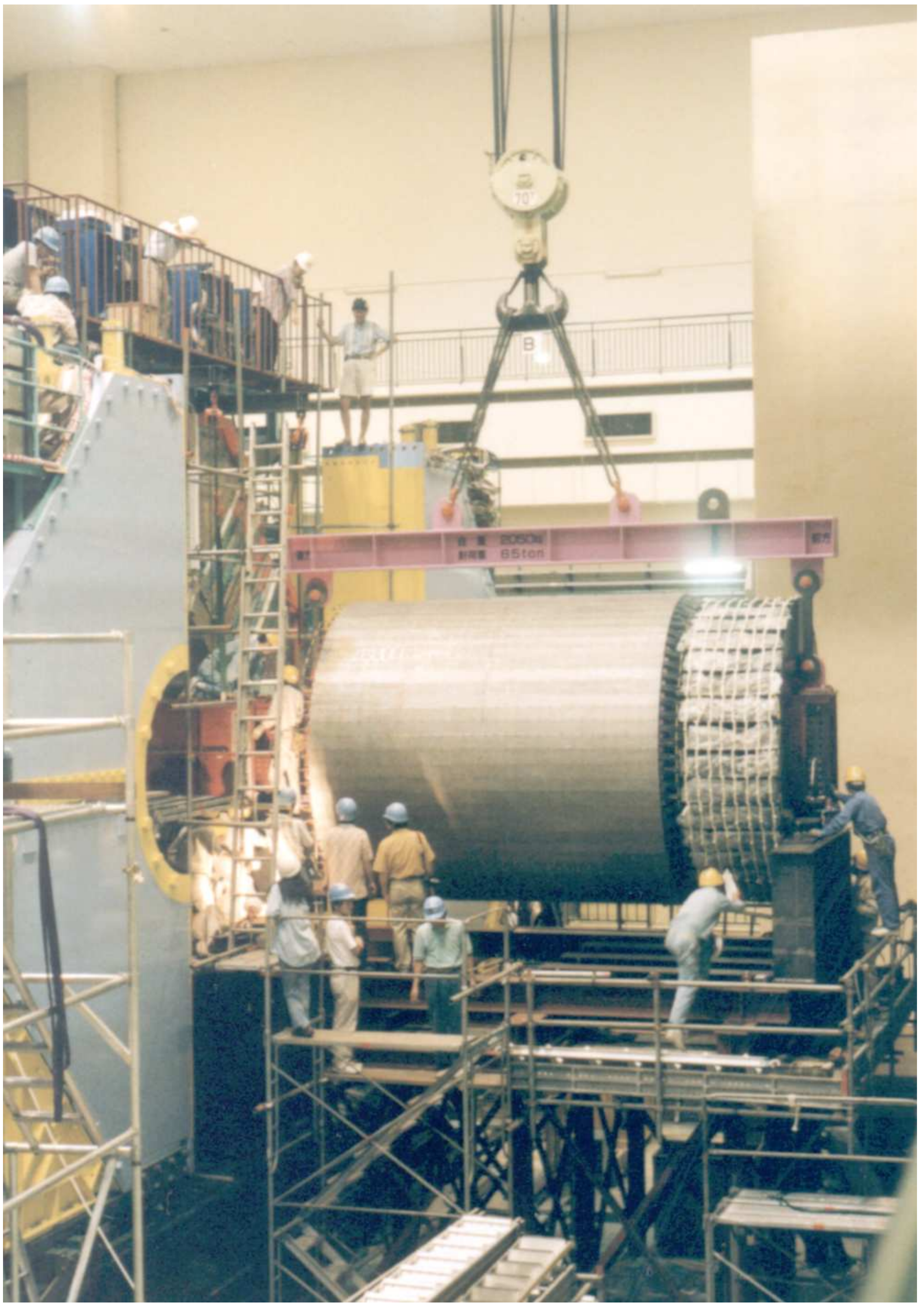

Figure 8.1: Installation of the BELLE calorimeter.

The energy linearity of the calorimeter is -3 ± 2 % for energies from 20 MeV to 5.4 GeV with the central value of $-$ 3 % which is due to the average shower leakage. The GEANT simulation did not reproduce the linearity at the lower energies than 100 MeV. The difference is almost 2 % and it looks there is still some effect that is not included in GEANT at the low energy. It is emphasized that this is the first measurement of the linearity for such a wide energy range by the photon beam. We observed that it is not necessary to correct the electronics non-linearity because our electronics has an excellent linear response. Non-uniformity of light output affects the linearity but it is only within ± 1 %.

In analyzing the beam test data, we established a clustering method. We used the sum of 5 × 5 counters with 0.5 MeV threshold to obtain the cluster energy with good resolution and linearity described above. It helps us to detect the electron, γ, and also π^0 with good efficiency. We estimated the average detection efficiency of 63 % for γ and 41.6 % for π^0 for γ's and π^0's from $B\bar{B}$ decays by the GEANT simulation.

We installed the barrel calorimeter into BELLE and started the system test by using the cosmic ray in October 1998. The signal from all counters are checked. It was confirmed that all counters and electronics work correctly except two out of 6624 counters which have no response from one of the two preamplifiers. Fig. 8.2 is an example of the cosmic ray triggered event and recorded by the barrel calorimeter. A clear energy deposit caused by a cosmic ray is seen and there are no strange hits in other counters. We measured the noise level of all the counters. The average noise is 217.0 ± 33.09 keV as shown in Fig. 8.4[71]. We confirmed the whole system is healthy now and will work well in the BELLE experiment which will start from April 1999.

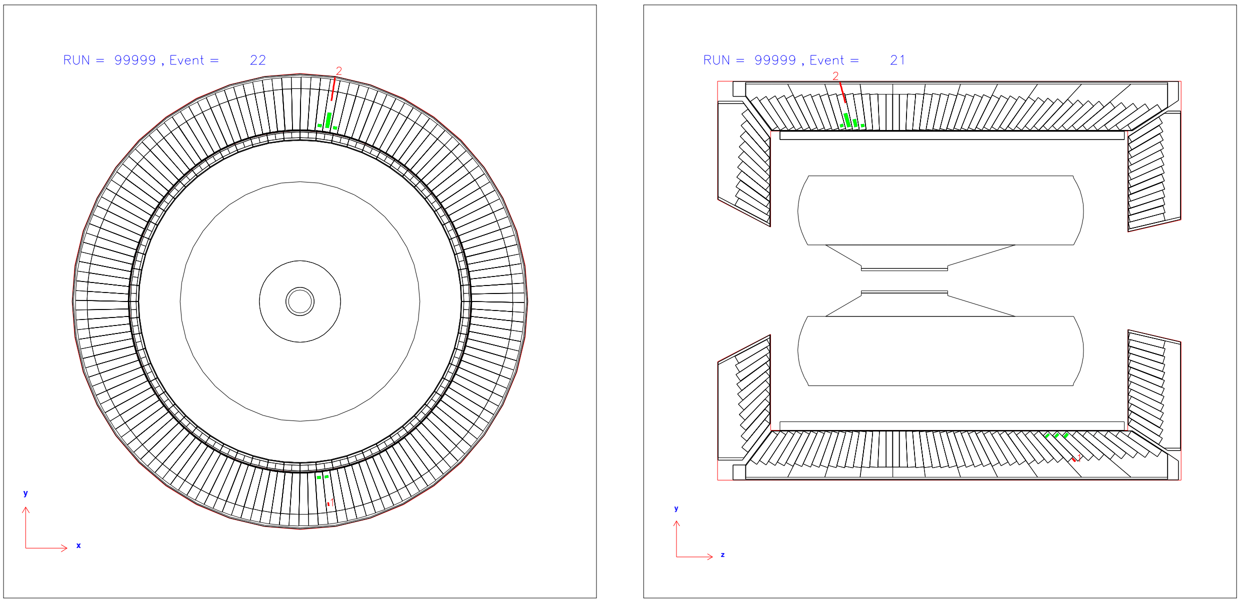
RUN = 99999 , Event = 22
2
1
y
x
RUN = 99999 , Event = 21
2
1
y
z

Figure 8.2: The first cosmic ray event seen after installation of the CsI(Tℓ) calorimeter into the BELLE detector (Oct. 1998)

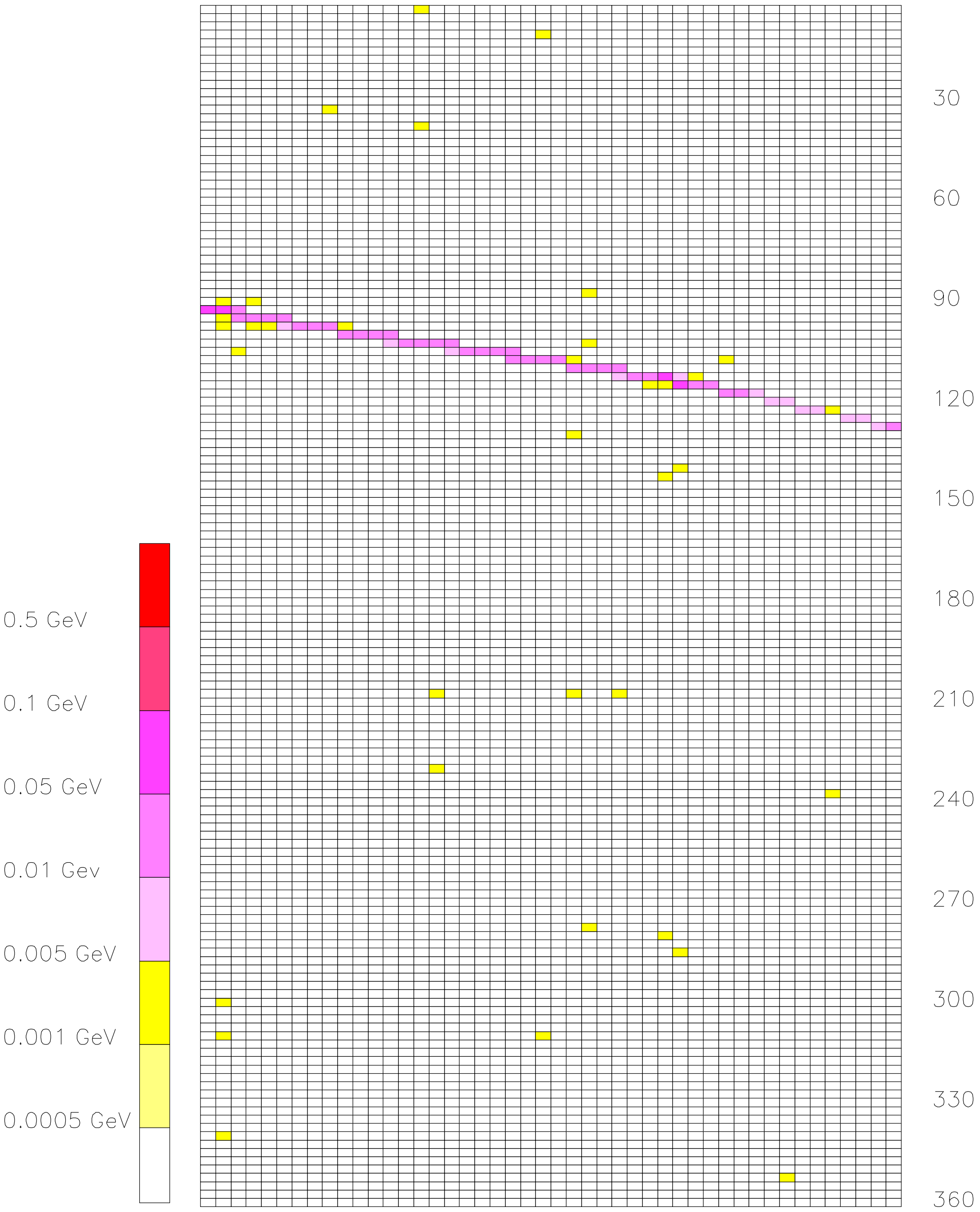

Figure 8.3: The first cosmic ray event seen after installation of the CsI(Tℓ) calorimeter into the BELLE detector (Oct. 1998)

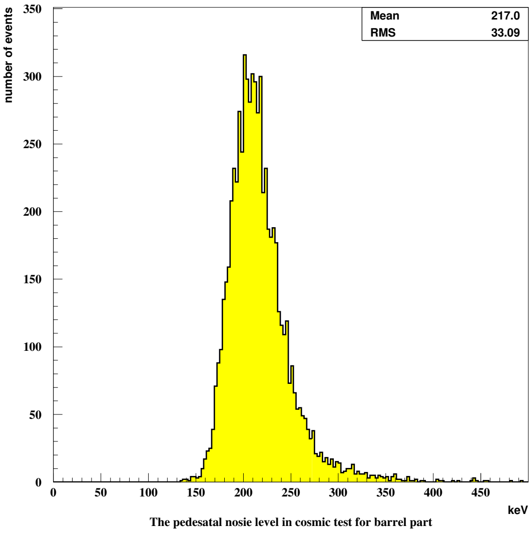

Figure 8.4: Distribution of the noise level for all the barrel counters after installation.

Appendix A

Chronicles of CsI(Tℓ) Crystal Production for BELLE [*]

RU : Production effort in Russia and Ukraine.

Institute for Single Crystals (ISC) in Kharkov produced crystal ingots and made a mechanical processing. Raremetal Factory (RMF) in Novosibirsk supplied CsI powder. Ise Chemical in Japan supplied the Iodine. Hydrogen iodide (HI) was produced in Galogen in Ural mountains. Budker Institute for Nuclear Study (BINP) in Novosibirsk was in charge for the overall organization of above mentioned enterprises. (see Fig. A.1(a))

CH : Production effort in China.

The Crystal production R/D was performed by Shanghai Institute of Ceramics (SIC) and by Beijing Glass Research Institute (BGRI). The most of crystal production was done by SIC. Institute for High Energy Physics (IHEP) in Beijing participated in the initial stage of organization. Raw CsI and TlI materials were supplied by Chemetall (CM) in Germany. (see Fig. A.1(b))

---

[*] This record was prepared with the help of M.Fukushima and M.H.Lee who worked for the management and technical coordination of the crystal production for BELLE.

(a)

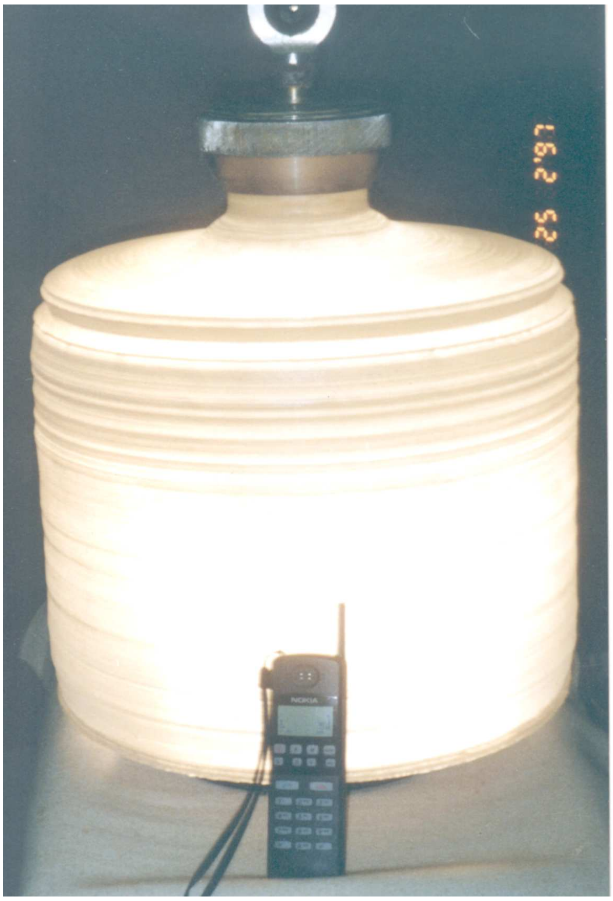

(b)

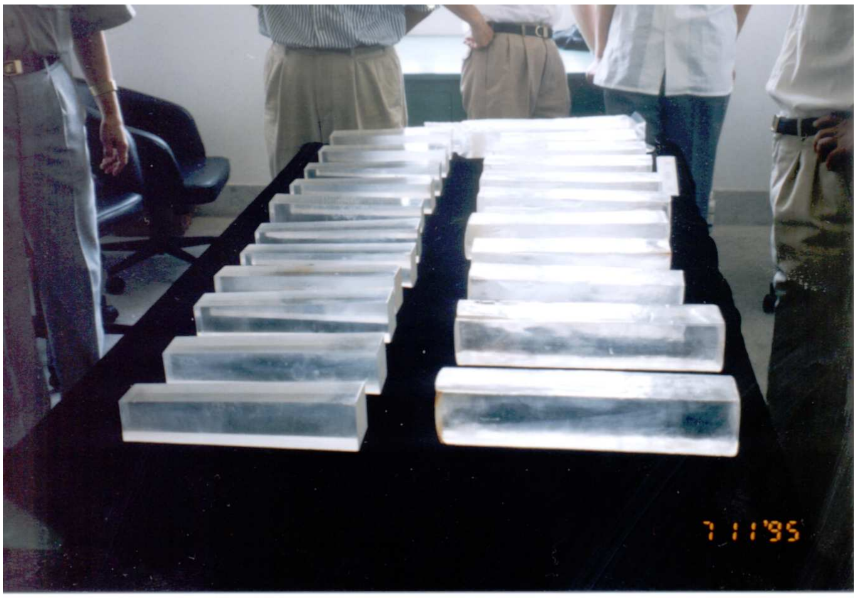

Figure A.1: Ingots of CsI(Tℓ) crystals produce by (a) Institute for Single Crystals in Ukraine and (b)Shanghai Institute of Ceramics. The Chinese crystals are grown by the Bridgman method. The Ukrainian crystals are produced by the Czochralski method. The growth speed of the crystal is ~ 1 mm/hour in either method.

FR :	Production effort in France. Crystals were grown by Quartz et Silice (QS) company in France. Later the company changed the name to Crismatec/Bicron.
KE :	Activity at KEK. Most of commercial and logistic problems between KEK and producers in RU, CH and FR were handled by Toyota Tsusho Corporation (TTC) in Tokyo.

⋆⋆

1992 Sep	FR	KEK made a purchase order of 120 pcs to QS.
1992 Nov	FR	First 10 pcs delivered from QS and tested at KEK. Some crystals had pink color, polycrystalline boundaries in the middle of the crystal, and wide pedestal values due to phosphorescence.
1992 May	FR	Nine crystals were replaced by QS due to boundaries and non-uniformity.
1992 May	CH	Visit to IHEP and crystal producers in Beijing. This is the first contact with Chinese crystal growers.
1992 Jul	RU	Visit to BINP and ISC. This is the first contact with Russian and Ukrainian crystal suppliers.
1992 Oct	RU	First 10 test pcs delivered from BINP. All had yellowish colors and the light output (LO) was 40% of specification. This was improved for the subsequent production.
1993 Aug	FR	Delivery of 120 pcs by QS completed.
1993 Dec	RU	Production baseline for barrel crystals agreed between BINP, ISC and KEK.

1994 May	CH	R/D in China for CsI(Tℓ) production started at SIC and BGRI.
1994 Aug	CH	First large CsI(Tℓ) sample from SIC. Bubbles, brown coloration and opaqueness observed. LO was half of specification.
1994 Oct	RU	First mass produced 120 pcs from BINP delivered to KEK. LO and uniformity specification mostly satisfied. Mechanical tolerance was problematic. Lots of mechanical damages were caused on the crystal during the transport from BINP to KEK.
1995 Feb	CH	Transparency of SIC crystals improved but still LO is 80% of specification.
1995 Apr	CH	Three pcs with good uniformity delivered from SIC. LO is 93% of specification.
1995 Aug	RU	Severe damages were caused on the crystal surface by water condensation for 100 pcs from BINP during the transport between BINP-KEK.
1995 Nov	RU	First beam test at BINP. Data taking was repeated in March, 1996.
1995 Sep	CH	Twenty pcs delivered from SIC. Good uniformity but LO is 86% of specification. Severe radiation damage observed by ^{60}Co irradiation for SIC crystals. Decrease of LO by 19% after 10 rad irradiation.
1995 Oct	CH	Small test crystals grown with scavenger were reported significantly radiation harder by Igarashi (KEK) and Zhong (IHEP).
1995 Nov	CH	Growth of large CsI(Tℓ) crystals with scavenger decided by SIC.
1996 Jan	FR	First 55 pcs for the other of 900 barrel crystals delivered by QS. Specifications satisfied.

1996 Jan	CH	Discussion on radiation hardness at SIC. CsI powder quality, baking temperature dependence, use of vacuum furnace (at BGRI) etc. were discussed.
1996 Feb	CH	Five pcs from SIC with scavenger were found to satisfy radiation hardness specification. Contamination of dirt by scavenger was noticeable for these crystals but it gradually improved for later production.
1996 Jul	CH	Lumping of CsI powder from CM caused severe loss in crystal production yield at SIC. Inefficient baking of lumped material was suspected.
1996 Sep	RU	CsI(Na) problem for BINP crystals was disclosed. Certain fraction of BINP crystals from BINP was known to show double photopeaks for 662 keV gamma rays from ^{137}Cs. The problem was traced that a part of CsI crystal block has only small amount of Sodium impurity and no Thallium activator doped. All crystals delivered to KEK from BINP (2700 pcs) were checked and about 200 pcs were found bad.
1996 Oct	CH	Mass production started at SIC.
1997 Feb	CH	Twenty pcs out of 239 pcs delivered from SIC returned for replacement. These are mostly by bad uniformity and cracks.
1997 Mar	FR	Delivery of 900 pcs from QS completed.
1997 Mar	RU	Total 216 pcs were shipped back to BINP for replacement. They were mostly CsI(Na) contaminated crystals.
1997 Aug	RU	Second beam test at BINP until November 1997. During the beam test, the silicone rubber glue joint was found unstable against temperature change.
1997 Dec	KE	Regluing of 6000 barrel crystals by epoxy glue took until February 1998.
1998 Feb	KE	Installation of barrel crystals into the support structure continued until May 1998.

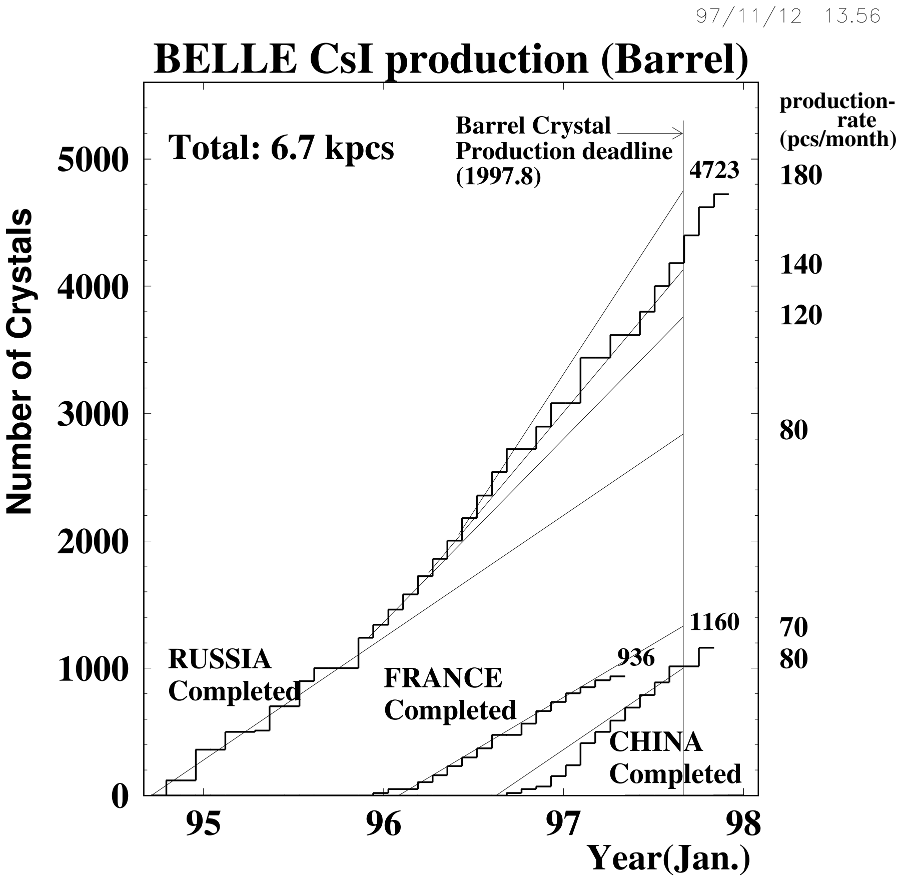

Figure A.2: Crystal delivery for BARREL.

1998 Feb	CH	“Pink” crystals and low LO caused by the change of material processing method at CM. Only 30% yield was achieved by these materials.
1998 May	KE	Break down of completed barrel calorimeter support structure.
1998 Jul	CH	The last crystals from SIC were delivered to KEK.
1998 Aug	KE	Delivery of new barrel support structure. Reinstallation of barrel counters was done in less than 50 days.
1998 Sep	RU	The last crystals from BINP were delivered to KEK.
1998 Sep	KE	Installation of barrel calorimeter to BELLE.

Appendix B

CsI(Tℓ) Crystal Size

Crystal No.	No.1	No.2	No.3	No.4	No.5	No.6	No.7	No.8
A(mm)	66.962	66.953	66.916	66.853	66.768	66.659	66.528	66.376
B(mm)	66.962	67.018	67.109	67.176	67.216	67.232	67.221	67.188
H(mm)	54.500	67.690	67.652	67.589	67.502	67.391	67.258	67.104
a(mm)	53.870	53.870	53.871	53.871	53.872	53.872	53.873	53.873
b(mm)	53.870	53.923	54.027	54.131	54.234	54.336	54.435	54.533
h(mm)	54.500	54.513	54.513	54.513	54.513	54.513	54.512	54.512
α(deg)	0.0000	0.0275	0.0821	0.1366	0.1905	0.2436	0.2957	0.3467
β(deg)	1.2500	1.2503	1.2490	1.2455	1.2395	1.2313	1.2208	1.2083
β'(deg)	1.2500	1.2491	1.2455	1.2395	1.2313	1.2209	1.2083	1.1938
γ(deg)	0.0000	1.2581	1.2545	1.2485	1.2402	1.2296	1.2170	1.2023
Volume(cc)	987.8	1112.2	1112.4	1112.2	1111.5	1110.4	1108.8	1106.8
Weight(kg)	4.455	5.016	5.017	5.016	5.013	5.008	5.001	4.992

Table B.1: Barrel crystal size 1.

Crystal No.	No.9	No.10	No.11	No.12	No.13	No.14	No.15	No.16
A(mm)	66.204	66.015	65.808	65.588	65.354	65.108	64.854	64.590
B(mm)	67.131	67.051	66.951	66.830	66.692	66.538	66.368	66.186
H(mm)	66.931	66.739	66.531	66.308	66.071	65.823	65.565	65.299
a(mm)	53.873	53.874	53.874	53.875	53.875	53.875	53.876	53.876
b(mm)	54.628	54.720	54.810	54.896	54.979	55.060	55.135	55.209
h(mm)	54.512	54.511	54.511	54.511	54.510	54.510	54.509	54.509
α(deg)	0.3963	0.4448	0.4917	0.5369	0.5801	0.6221	0.6618	0.7002
β(deg)	1.1938	1.1774	1.1592	1.1395	1.1184	1.0959	1.0725	1.0481
β'(deg)	1.1774	1.1592	1.1395	1.1184	1.0960	1.0725	1.0482	1.0230
γ(deg)	1.1858	1.1675	1.1477	1.1264	1.1039	1.0802	1.0557	1.0303
Volume(cc)	1104.4	1101.7	1098.6	1095.3	1091.6	1087.8	1083.7	1079.4
Weight(kg)	4.981	4.969	4.955	4.940	4.923	4.906	4.887	4.868

Table B.2: Barrel crystal size 2.

Crystal No.	No.17	No.18	No.19	No.20	No.21	No.22	No.23	No.24
A(mm)	64.320	64.044	63.765	63.483	63.200	62.918	62.635	62.355
B(mm)	65.991	65.787	65.574	65.354	65.127	64.896	64.662	64.426
H(mm)	65.026	64.748	64.466	64.181	63.896	63.610	63.325	63.042
a(mm)	53.877	53.877	53.877	53.877	53.877	53.878	53.878	53.878
b(mm)	55.278	55.344	55.406	55.466	55.521	55.573	55.623	55.669
h(mm)	54.509	54.508	54.508	54.507	54.507	54.506	54.506	54.506
α(deg)	0.7539	0.7713	0.8037	0.8348	0.8639	0.8910	0.9170	0.9409
β(deg)	1.0166	0.9971	0.9709	0.9441	0.9172	0.8902	0.8631	0.8362
β'(deg)	0.9971	0.9708	0.9441	0.9172	0.8902	0.8632	0.8362	0.8094
γ(deg)	1.0042	0.9778	0.9508	0.9237	0.8965	0.8693	0.8421	0.8151
Volume(cc)	1075.0	1070.5	1065.9	1061.2	1056.5	1051.8	1047.1	1042.4
Weight(kg)	4.848	4.828	4.807	4.786	4.765	4.744	4.722	4.701

Table B.3: Barrel crystal size 3.

Crystal No.	No.25	No.26	No.27	No.28	No.29
A(mm)	62.077	61.803	61.533	61.267	61.006
B(mm)	64.189	63.951	63.715	63.480	63.247
H(mm)	62.762	62.485	62.212	61.944	61.682
a(mm)	53.878	53.879	53.879	53.879	53.879
b(mm)	55.713	55.752	55.790	55.826	55.859
h(mm)	54.505	54.505	54.505	54.504	54.504
α(deg)	0.9638	0.9849	1.0047	1.0234	1.0406
β(deg)	0.8093	0.7829	0.7567	0.7309	0.7055
β'(deg)	0.7829	0.7566	0.7309	0.7055	0.6805
γ(deg)	0.7884	0.7620	0.7359	0.7104	0.6854
Volume(cc)	1037.7	1033.1	1028.5	1024.1	1019.7
Weight(kg)	4.680	4.659	4.639	4.619	4.599

Table B.4: Barrel crystal size 4.

Crystal No.	No.1	No.2	No.3	No.4	No.5	No.6	No.7	No.8
A(mm)	56.514	56.764	53.464	53.638	53.714	53.714	53.464	75.880
B(mm)	58.740	58.990	55.728	55.978	55.978	55.978	55.728	79.456
C(mm)	60.333	60.333	62.483	62.492	60.456	62.483	60.465	61.072
D(mm)	60.333	60.333	60.465	62.492	62.483	60.456	62.483	63.321
a(mm)	49.656	49.906	46.884	47.068	47.135	47.135	46.884	66.458
b(mm)	51.614	51.864	48.870	49.120	49.120	49.120	48.870	69.592
c(mm)	53.048	53.048	54.836	54.845	53.057	54.836	53.066	53.501
d(mm)	53.048	53.048	53.066	54.845	54.836	53.057	54.836	55.471
H_{aA}(mm)	3.707	3.707	3.882	4.010	3.883	3.882	3.883	4.061
H_{dD}(mm)	3.497	3.497	3.360	3.359	3.359	3.360	3.359	4.825
dg13(mm)	73.328	73.501	71.465	72.938	72.931	71.626	72.766	86.497
dg24(mm)	73.328	73.501	72.766	72.938	71.626	72.931	71.465	87.771
dg57(mm)	83.425	83.598	81.458	83.113	83.106	81.619	82.942	98.750
dg68(mm)	83.425	83.598	82.942	83.113	81.619	83.106	81.458	100.205
α_1(deg)	91.057	91.057	93.235	91.072	88.910	93.234	88.910	91.633
α_2(deg)	88.943	88.943	88.928	88.928	88.928	88.928	88.928	86.745
α_3(deg)	88.943	88.943	88.928	88.928	88.928	88.928	88.928	89.988
α_4(deg)	91.057	91.057	88.910	91.072	93.234	88.910	93.235	91.633
Volume(cc)	923	927	894	914	898	897	894	1308
Weight(kg)	4.16	4.18	4.03	4.12	4.05	4.05	4.03	5.90

Table B.5: Forward endcap crystal size 1.

Crystal No.	No.9	No.10	No.11	No.12	No.13	No.14	No.15	No.16
A(mm)	76.130	76.130	75.880	71.360	71.610	66.926	67.176	62.366
B(mm)	79.707	79.707	79.456	74.866	75.116	70.486	70.736	66.143
C(mm)	63.328	61.072	63.321	60.667	60.667	60.769	60.769	63.663
D(mm)	61.072	63.328	61.072	60.667	60.667	60.769	60.769	63.663
a(mm)	66.708	66.708	66.458	62.378	62.628	58.397	58.648	54.322
b(mm)	69.842	69.842	69.592	65.444	65.694	61.504	61.754	57.614
c(mm)	55.478	53.501	55.471	53.046	53.046	53.047	53.047	55.483
d(mm)	53.501	55.478	53.501	53.046	53.046	53.047	53.047	55.483
H_{aA}(mm)	4.061	4.061	4.061	3.942	3.942	3.988	3.988	4.211
H_{dD}(mm)	4.825	4.825	4.825	4.603	4.603	4.380	4.379	4.145
dg13(mm)	87.970	86.693	87.771	83.043	83.236	80.035	80.223	78.792
dg24(mm)	86.693	87.970	86.497	83.043	83.236	80.035	80.223	78.792
dg57(mm)	100.404	98.947	100.205	94.989	95.182	91.707	91.895	90.433
dg68(mm)	98.947	100.404	98.750	94.989	95.182	91.707	91.895	90.432
α_1(deg)	91.633	91.633	91.633	91.656	91.656	91.679	91.678	91.700
α_2(deg)	89.988	86.746	89.988	88.344	88.344	88.321	88.322	88.300
α_3(deg)	86.746	89.988	86.745	88.344	88.344	88.322	88.322	88.300
α_4(deg)	91.633	91.633	91.633	91.656	91.656	91.678	91.678	91.700
Volume(cc)	1312	1313	1307	1190	1195	1107	1112	1075
Weight(kg)	5.92	5.92	5.89	5.37	5.39	4.99	5.02	4.85

Table B.6: Forward endcap crystal size 2.

Crystal No.	No.17	No.18	No.19	No.20	No.21	No.22	No.23	No.24
A(mm)	62.616	57.981	58.232	53.661	53.710	53.913	53.913	53.661
B(mm)	66.394	61.642	61.892	57.369	57.620	57.620	57.620	57.369
C(mm)	63.663	60.968	60.968	64.366	64.382	61.073	64.366	61.089
D(mm)	63.663	60.969	60.968	61.089	64.382	64.366	61.073	64.366
a(mm)	54.572	50.413	50.664	46.579	46.654	46.830	46.830	46.579
b(mm)	57.864	53.598	53.848	49.800	50.050	50.050	50.050	49.800
c(mm)	55.483	53.046	53.046	55.920	55.935	53.059	55.920	53.074
d(mm)	55.483	53.046	53.046	53.074	55.935	55.920	53.059	55.920
H$_{aA}$(mm)	4.211	4.077	4.077	4.326	4.549	4.324	4.325	4.324
H$_{dD}$(mm)	4.145	3.905	3.905	3.664	3.664	3.664	3.664	3.664
dg13(mm)	78.969	74.269	74.445	71.669	73.917	73.906	71.827	73.743
dg24(mm)	78.969	74.269	74.445	73.743	73.917	71.827	73.906	71.669
dg57(mm)	90.611	85.388	85.564	82.525	85.087	85.075	82.682	84.911
dg68(mm)	90.611	85.389	85.564	84.911	85.087	82.682	85.075	82.525
α_1(deg)	91.700	91.721	91.720	95.240	91.740	88.239	95.239	88.239
α_2(deg)	88.300	88.279	88.280	88.261	88.260	88.261	88.261	88.261
α_3(deg)	88.300	88.280	88.280	88.261	88.260	88.261	88.261	88.261
α_4(deg)	91.700	91.720	91.720	88.239	91.740	95.239	88.239	95.240
Volume(cc)	1080	957	961	917	949	923	921	919
Weight(kg)	4.87	4.32	4.34	4.14	4.28	4.16	4.15	4.14

Table B.7: Forward endcap crystal size 3.

Crystal No.	No.25	No.26	No.27	No.28	No.29	No.30	No.31	No.32
A(mm)	74.160	74.410	74.410	74.160	67.747	67.998	61.335	61.586
B(mm)	79.958	80.209	80.209	79.958	73.437	73.688	67.153	67.404
C(mm)	60.263	63.940	60.263	63.928	61.230	61.230	64.221	61.316
D(mm)	63.928	60.263	63.940	60.263	61.230	61.230	61.328	64.221
a(mm)	64.320	64.570	64.570	64.320	58.667	58.918	53.040	53.290
b(mm)	69.349	69.600	69.600	69.349	63.596	63.846	58.073	58.324
c(mm)	52.279	55.470	52.279	55.459	53.044	53.044	55.568	53.055
d(mm)	55.459	52.279	55.470	52.279	53.044	53.044	53.067	55.568
H_{aA}(mm)	4.466	4.466	4.466	4.466	4.308	4.308	4.521	4.521
H_{dD}(mm)	5.120	5.120	5.120	5.120	4.735	4.735	4.350	4.351
dg13(mm)	84.732	87.039	84.929	86.838	80.899	81.089	76.810	78.649
dg24(mm)	86.838	84.929	87.039	84.732	80.900	81.089	78.471	76.983
dg57(mm)	97.686	100.314	97.883	100.113	93.404	93.594	88.795	90.894
dg68(mm)	100.113	97.883	100.314	97.686	93.404	93.594	90.716	88.969
α_1(deg)	92.636	92.637	92.637	92.637	92.664	92.662	95.386	89.987
α_2(deg)	84.739	89.988	84.739	89.988	87.336	87.338	87.314	87.313
α_3(deg)	89.988	84.739	89.988	84.739	87.338	87.338	87.313	87.312
α_4(deg)	92.637	92.637	92.637	92.636	92.662	92.662	89.988	95.388
Volume(cc)	1281	1283	1286	1278	1140	1145	1050	1057
Weight(kg)	5.78	5.79	5.80	5.76	5.14	5.16	4.74	4.77

Table B.8: Forward endcap crystal size 4.

Crystal No.	No.33	No.34	No.35	No.36	No.37	No.38	No.39
A(mm)	61.586	61.335	73.337	73.588	73.337	64.956	65.206
B(mm)	67.404	67.153	81.303	-	81.303	72.757	73.008
C(mm)	64.221	61.328	61.618	61.633	64.177	61.444	61.444
D(mm)	61.316	64.221	64.177	61.633	61.618	61.444	61.444
a(mm)	53.290	53.040	63.364	63.614	63.364	56.050	56.300
b(mm)	58.324	58.073	70.250	-	70.250	62.785	63.036
c(mm)	55.568	53.067	53.255	53.270	55.465	53.043	53.043
d(mm)	53.055	55.568	55.465	53.270	53.255	53.043	53.043
B_7=B_9(mm)	-	-	-	40.858	-	-	-
b_2=b_4(mm)	-	-	-	35.321	-	-	-
H_{aA}(mm)	4.521	4.521	4.679	4.679	4.679	4.492	4.492
H_{dD}(mm)	4.351	4.351	5.271	5.272	5.272	4.729	4.729
dg13(mm)	76.983	78.471	85.302	85.507	86.800	79.578	79.765
dg24(mm)	78.649	76.810	86.800	85.507	85.302	79.578	79.765
dg57(mm)	88.969	90.716	98.714	98.921	100.449	92.203	92.390
dg68(mm)	90.894	88.795	100.449	98.921	98.714	92.202	92.390
α_1(deg)	95.388	89.988	93.613	93.613	93.613	93.639	93.640
α_2(deg)	87.312	87.313	84.588	-	88.186	86.361	86.360
α_3(deg)	87.313	87.314	88.186	-	84.588	86.360	86.360
α_4(deg)	89.987	95.386	93.613	93.613	93.613	93.640	93.640
α_2'(deg)	-	-	-	91.785	-	-	-
α_3'(deg)	-	-	-	91.785	-	-	-
α_9(deg)	-	-	-	169.203	-	-	-
Volume(cc)	1054	1052	1293	1316	1290	1106	1111
Weight(kg)	4.76	4.75	5.83	5.94	5.82	4.99	5.01

Table B.9: Forward endcap crystal size 5.

Crystal No.	No.1	No.2	No.3	No.4	No.5	No.6	No.7	No.8
A(mm)	59.870	60.120	55.740	55.944	55.990	55.990	55.740	77.984
B(mm)	61.610	61.860	57.576	57.826	57.826	57.826	57.576	80.864
C(mm)	64.566	64.566	66.702	66.709	65.085	66.702	65.092	63.837
D(mm)	64.566	64.566	65.092	66.709	66.702	65.085	66.702	65.588
a(mm)	49.722	49.972	45.915	46.126	46.165	46.165	45.915	63.774
b(mm)	51.170	51.420	47.428	47.678	47.678	47.678	47.428	66.130
c(mm)	53.673	53.673	55.010	55.017	53.677	55.010	53.684	52.225
d(mm)	53.673	53.673	53.684	55.017	55.010	53.677	55.010	53.657
H_{aA}(mm)	5.515	5.515	5.913	6.057	5.913	5.913	5.913	6.124
H_{dD}(mm)	5.148	5.148	4.994	4.994	4.993	4.994	4.993	7.239
dg13(mm)	73.655	73.826	71.131	72.292	72.287	71.290	72.125	83.317
dg24(mm)	73.655	73.826	72.125	72.292	71.290	72.287	71.131	84.247
dg57(mm)	88.642	88.813	86.292	87.664	87.659	86.451	87.497	101.866
dg68(mm)	88.642	88.813	87.497	87.664	86.451	87.659	86.292	103.002
α_1(deg)	90.773	90.773	92.463	90.808	89.153	92.463	89.152	91.267
α_2(deg)	89.227	89.227	89.192	89.192	89.193	89.192	89.193	87.493
α_3(deg)	89.227	89.227	89.193	89.192	89.192	89.193	89.192	89.975
α_4(deg)	90.773	90.773	89.152	90.808	92.463	89.153	92.463	91.266
Volume(cc)	990	995	945	962	949	949	945	1305
Weight(kg)	4.47	4.49	4.26	4.34	4.28	4.28	4.26	5.88

Table B.10: Backward endcap crystal size 1.

Crystal No.	No.9	No.10	No.11	No.12	No.13	No.14	No.15	No.16
A(mm)	78.234	78.234	77.984	72.170	72.420	66.518	66.768	61.008
B(mm)	81.114	81.114	80.864	75.221	75.472	69.722	69.972	64.366
C(mm)	65.593	63.837	65.588	66.125	66.125	66.653	66.653	67.180
D(mm)	63.837	65.593	63.837	66.125	66.125	66.653	66.653	67.180
a(mm)	64.024	64.024	63.774	58.535	58.786	53.506	53.756	48.672
b(mm)	66.380	66.380	66.130	61.010	61.260	56.086	56.336	51.354
c(mm)	53.662	52.225	53.657	53.664	53.664	53.662	53.662	53.658
d(mm)	52.225	53.662	52.225	53.664	53.664	53.662	53.662	53.658
H_{aA}(mm)	6.124	6.124	6.124	6.389	6.389	6.654	6.654	6.917
H_{dD}(mm)	7.239	7.239	7.239	6.964	6.962	6.664	6.664	6.339
dg13(mm)	84.443	83.512	84.247	80.318	80.505	76.684	76.863	73.339
dg24(mm)	83.512	84.443	83.317	80.319	80.505	76.684	76.863	73.339
dg57(mm)	103.198	102.061	103.002	99.001	99.187	95.291	95.470	91.869
dg68(mm)	102.061	103.198	101.866	99.000	99.187	95.291	95.470	91.869
α_1(deg)	91.266	91.266	91.266	91.322	91.321	91.377	91.377	91.432
α_2(deg)	89.974	87.493	89.975	88.678	88.679	88.623	88.623	88.568
α_3(deg)	87.493	89.974	87.493	88.679	88.679	88.623	88.623	88.568
α_4(deg)	91.266	91.266	91.267	91.321	91.321	91.377	91.377	91.432
Volume(cc)	1309	1310	1304	1210	1215	1113	1118	1027
Weight(kg)	5.91	5.91	5.88	5.46	5.48	5.02	5.04	4.63

Table B.11: Backward endcap crystal size 2.

Crystal No.	No.17	No.18	No.19	No.20	No.21	No.22	No.23	No.24
A(mm)	61.258	55.625	55.720	55.875	55.875	55.625	75.884	76.134
B(mm)	64.616	59.136	59.386	59.386	59.386	59.136	81.310	81.561
C(mm)	67.180	70.668	70.681	67.714	70.668	67.727	64.965	68.201
D(mm)	67.180	67.727	70.681	70.668	67.714	70.668	68.191	64.965
a(mm)	48.922	44.018	44.144	44.268	44.268	44.018	59.650	59.900
b(mm)	51.604	46.800	47.050	47.050	47.050	46.800	63.916	64.167
c(mm)	53.658	56.009	56.022	53.668	56.009	53.681	51.094	53.642
d(mm)	53.658	53.681	56.022	56.009	53.668	56.009	53.631	51.094
H_{aA}(mm)	6.917	7.473	7.789	7.472	7.473	7.472	7.613	7.613
H_{dD}(mm)	6.339	5.988	5.987	5.988	5.988	5.987	8.417	8.417
dg13(mm)	73.510	70.297	72.218	72.208	70.448	72.051	80.088	82.001
dg24(mm)	73.510	72.051	72.218	70.448	72.208	70.297	81.805	80.281
dg57(mm)	92.040	88.748	91.130	91.120	88.900	90.963	101.862	104.241
dg68(mm)	92.040	90.963	91.130	88.900	91.120	88.748	104.044	102.055
α_1(deg)	91.432	94.516	91.486	88.455	94.516	88.455	92.307	92.307
α_2(deg)	88.568	88.514	88.514	88.514	88.514	88.514	85.420	89.966
α_3(deg)	88.568	88.514	88.514	88.514	88.514	88.514	89.966	85.419
α_4(deg)	91.432	88.455	91.486	94.516	88.455	94.516	92.307	92.308
Volume(cc)	1032	975	1005	980	979	977	1274	1277
Weight(kg)	4.65	4.40	4.53	4.42	4.42	4.40	5.74	5.76

Table B.12: Backward endcap crystal size 3.

Crystal No.	No.25	No.26	No.27	No.28	No.29	No.30
A(mm)	76.134	75.884	68.318	68.568	60.939	61.190
B(mm)	81.561	81.310	73.837	74.088	66.660	66.910
C(mm)	64.965	68.191	66.362	66.362	66.808	66.808
D(mm)	68.201	64.965	66.362	66.362	66.808	66.808
a(mm)	59.900	59.650	53.293	53.544	47.198	47.448
b(mm)	64.167	63.916	57.602	57.852	51.634	51.884
c(mm)	51.094	53.631	51.814	51.814	51.810	51.810
d(mm)	53.642	51.094	51.814	51.814	51.810	51.810
H_{aA}(mm)	7.613	7.613	7.593	7.593	7.801	7.801
H_{dD}(mm)	8.417	8.417	7.822	7.821	7.198	7.199
dg13(mm)	80.281	81.805	75.858	76.041	71.564	71.736
dg24(mm)	82.001	80.088	75.858	76.041	71.564	71.736
dg57(mm)	102.055	104.044	97.203	97.386	92.333	92.507
dg68(mm)	104.241	101.862	97.202	97.386	92.334	92.507
α_1(deg)	92.308	92.307	92.384	92.383	92.454	92.454
α_2(deg)	85.419	89.966	87.616	87.617	87.546	87.546
α_3(deg)	89.966	85.420	87.617	87.617	87.546	87.546
α_4(deg)	92.307	92.307	92.383	92.383	92.454	92.454
Volume(cc)	1279	1272	1128	1133	1012	1016
Weight(kg)	5.77	5.74	5.09	5.11	4.56	4.58

Table B.13: Backward endcap crystal size 4.

Appendix C

Compton Fitting Function

We used the convolution of logarithmic Gaussian and the CsI response function for the fitting of the energy distribution of the backscattered Compton photons as follow;

$$\begin{aligned} F(\varepsilon) \;=\; & N \frac{1}{E_c^3} \frac{\sigma_E}{\eta} \sigma_0 \,\{\, (\, \frac{E_c^2}{2} \;-\; E_c \,(\, \varepsilon \;-\; \frac{\sigma_E}{\eta} \,) \;+\; (\, \varepsilon \;-\; \frac{\sigma_E}{\eta})^2 \,)\, f_1(\varepsilon) \\ & + \,(\, \exp(1.5\sigma_0^2)\, \frac{\sigma_E}{\eta} \,(\, -E_c \;+\; 2 \,(\, \varepsilon \;-\; \frac{\sigma_E}{\eta} \,)\,)\, f_2(\varepsilon) \\ & + \,(\, \exp(4\sigma_0^2) \,(\, \frac{\sigma_E}{\eta})^2 \,)\, f_3(\varepsilon) \,\} \\ & + N_B \,(\, 1 \;-\; \frac{\varepsilon - E_c}{E_c} \,) \end{aligned} \tag{C.1}$$

$$\sigma_0 = \frac{1}{\sqrt{ln4}} sinh^{-1}(\sqrt{ln4}\eta) \tag{C.2}$$

$$f_1(\varepsilon) = erf(\frac{ln(1 - \frac{\varepsilon - E_c}{\sigma_0}\eta) - \sigma_0^2}{\sqrt{2}\sigma_0}) \;+\; erf(\frac{ln((1 - \frac{\varepsilon}{\sigma_0}\eta) - \sigma_0^2}{\sqrt{2}\sigma_0}) \tag{C.3}$$

$$f_2(\varepsilon) = erf(\frac{ln(1 - \frac{\varepsilon - E_c}{\sigma_0}\eta) - 2\sigma_0^2}{\sqrt{2}\sigma_0}) \;+\; erf(\frac{ln((1 - \frac{\varepsilon}{\sigma_0}\eta) - 2\sigma_0^2}{\sqrt{2}\sigma_0}) \tag{C.4}$$

$$f_3(\varepsilon) = erf(\frac{ln(1 - \frac{\varepsilon - E_c}{\sigma_0}\eta) - 3\sigma_0^2}{\sqrt{2}\sigma_0}) \;+\; erf(\frac{ln((1 - \frac{\varepsilon}{\sigma_0}\eta) - 3\sigma_0^2}{\sqrt{2}\sigma_0}) \tag{C.5}$$

$$erf(x) = \frac{2}{\sqrt{\pi}} \int_0^x exp(-t^2) dt \tag{C.6}$$

where normalization factor N, Compton edge energy E_c and background N_B are for CsI response. And resolution σ_E and asymmetry η come from the logarithmic Gaussian.

Acknowledgment

I want to thank everyone who helped me.

I express my gratitude to my supervisor of Prof. S. Noguchi, Prof. H. Hayashii and Prof. N. Fujiwara for their understanding and support for my work. They guided me since I was under graduate student, and help to keep my interest in physics. I could not have joined the BELLE experiment and enjoyed the work in this group without their encouragement.

Since I have worked mainly at KEK, I have been under the care of the KEK staffs. Heartfelt thanks go to Prof. M. Fukushima. He was my adviser at KEK for over 5 years. He taught me how to do experiments, and admonished my way of thinking and working. I cannot find words to thank him. I will never forget his advises even after parting.

Dr. M. H. Lee has been my good adviser since the first year of my work at KEK. His honest opinions were very helpful.

I thank all of the Calorimeter group members of KEK, NWU, TIT and many foreign institutes. I am grateful to Prof. K. Tamai, Dr. H. Sagawa, Dr. T. Tsukamoto, Dr. B. G. Cheon, and Dr. K. Kaneyuki for their useful comment, suggestion and instruction. I want to thank BINP collaborators; Prof. A. E. Bondar, Prof. B. A. Shwartz, Dr. A. S. Kuzmin, Dr. L. V. Romanov and Dr. V. N. Zhilich for their kind help and hospitality during our beam test at Novosibirsk. And I thank for the discussion about the analysis.

Finally, I give my thanks to all the students who shared the office in Tsukuba Hall, for their friendship, encouragement and stimulation. I especially thank Mr. S. Ichizawa and Mr. C. S. Park for their help on software tasks. If they were not here, I could not smoothly finish anything. And I don't forget Mr. A. Satpathy's friendship as well as his physicistship. I wish all of you success in future.

Bibliography

[1] S. Weinberg, Phys. Rev. Lett.**19**(1967) 1264.

[2] A. Salam, 'Elementary Particle Theory', ed. N. Svarthholm(Almqvist and Wiksell, 1968).

[3] S. L. Glashow, J. Illiopoulos and L. Maiani, Phys.Rev.**D2**(1970) 1285.

[4] Eur. Phys. J. **C3**(1998) 117.

[5] M. Kobayashi and T. Maskawa, Prog. Theor. Phys. **49**(1973) 652.

[6] A. Carter and I. Sanda, Phys. Rev. Lett. **64**(1980) 952.

[7] A. Carter and I. Sanda, Phys. Rev. **D23**(1981) 1567.

[8] I. Bigi and A. Sanda, Nucl. Phys. **B193**(1981) 851.

[9] Letter of intent, KEK Report 94-2(1994).

[10] B Study of CP Vioration in B Messon Decays Technical Design Report (1995) KEK Report 95-1.

[11] BaBar Collab., Technical design report for the BaBar detector (1995).

[12] BaBar Collab.,Letter of intent, SLAC-443(1994).

[13] HERA-B Proposal, DESY-PRC 94/02.

[14] T. D. Lee and C. N. Yang, Phys. Rev.**104** (1956) 254.

[15] C. S. Wu, E. Ambler, R. W. Hayward, D. D. Hoppes and R. P. Hudson, Phys. Rev. **105**(1957) 1413.

[16] M. Goldhaber, L. Grodzins and A. W. Sunyar, Phys. Rev. **109** (1958) 1015.

[17] J. H. Christenson et al., Phys. Rev. Lett. **13** (1964) 138.

[18] L. Wolfenstein, Phys. Rev. Lett. **51** (1983) 1945.

[19] I. I. Bigi and A. I. Sanda, Phys. Lett. **194** (1987) 307.

[20] N. Cabbibo, Phys. Rev. Lett. **10** (1963) 531.

[21] H. Leutwyler and M. Roos, Z. Phys. **C25** (1984) 91.

[22] M. Bourquin et al., Z. Phys. **C21** (1983) 27.

[23] A. Sirlin, Phys. Rev. **D35** (1987) 3423.

[24] H. Abramowicz et al., Z. Phys. **C15** (1982) 19.

[25] S. Stone 'PROSPECTS FOR B-PHYSICS IN THE NEXT DECADE' HEPSY 96-01.

[26] R. Fulton et al., Phys. Rev. Lett. **64** (1999) 16.

[27] H. Albrechet et al., Phys. Lett. **B234** (1990) 409.

[28] S. Stone 'Semileptonic B Decay' World Scientific, Sigapore (1994) 349.

[29] M. Gaillard and B. Lee Phys. Rev. **D10** (1974) 897.

[30] J. Hagelin, Phys. Rev. **D20** (1979) 2893.

[31] A. Ali and A. Aydin, Nucl. Phys. **B148** (1979) 165.

[32] T. Brown and S. Pakvasa, Phys. Rev. **D31** (1985) 1661.

[33] S. Pakvasa, Phys. Rev. **D28** (1985) 2915.

[34] I. Bigi and A. Sanda, Phys. Rev. **D29** (1984) 1393.

[35] G. Buchalla, A. J. Buras and M. K. Harlander, Nucl. Phys. **B337** (1990) 313.

[36] I. I. Bigi and A. I. Sanda, Nucl. Phys., **B281** (1987) 41.

[37] M. Yamauchi, BELLE note No.116 (1996).

[38] KEKB B-FACTORY DESIGN REPORT (1995) KEK Report 95-7.

[39] BELLE Progress Report 1996 April - 1997 March (1997).

[40] Technical Design Report of BELLE SVD (1998).

[41] W. S. Huang et al., BELLE note No.94 (1995).

[42] R. Akhmetshin, BELLE note No.239 (1998).

[43] E. Bloom and C. Peck, Ann. Rev. Nucl. and Part. Sci.**33**,(1983) 143.

[44] M. A. Akrawy et al., Nucl. Inst. and Meth. **A290** (1990) 76.

[45] H. Burkhardt et al., Nucl. Inst. and Meth. **A268** (1988) 116.

[46] W. Hoffman et al., Nucl. Inst. and Meth. **163** (1979) 77.

[47] M. A. Schneegans et al.,Nucl. Inst. and Meth. **193** (1982) 445.

[48] C. Fabjan and R. Wigmans, Rept. Prog. Phys. **52** (1989) 1519.

[49] J. V. Allaby et al., Nucl. Inst. and Meth. **A281** (1989) 291.

[50] IEEE Trans. Nuclear Science **35** (1988) 105.

[51] Review of Particle Physics (1998) 156.

[52] GRACE in electronics Catalog.

[53] K. Kazui et al., Nucl. Inst. and Meth. **A 394** (1997) 46.

[54] '1992 Progress Report on B Physics Task Force Activities' KEK report 93-1.

[55] S. Gunji et al., Nucl. Inst. and Meth. **A 295** (1990) 400

[56] K. Tamai 'Results of Photo-diode Inspection'.

[57] M. Tanaka et al., IEEE Trans. Nucl. Sci., **41** (1994) 1208; KEK-Preprint 93-156.

[58] K. Tamai 'Preamprifier Inspection' (1997).

[59] LeCroy MQT300 manual.

[60] LeCroy OPERATOR'S MANUAL 'MODEL 1877S 96 CHANNEL FASTBUS TDC.

[61] K. Kazui 'Bachelor Thesis' (1995).

[62] T. W. Hur et al., BELLE note No.107 (1995).

[63] O. C. Allkofer et al., Phys. Let. **36B** (1971) 425.

[64] Y. Takeuchi et al., Nucl. Inst. and Meth. **328** (1993) 526.

[65] Nucl. Inst. and Meth. **A410** (1988) 179.

[66] W. R. Leo 'Techniques for Nuclear and Particle Physics Experiments'.

[67] E. Blucher et al, Nucl. Inst. and Meth. **A249** (1986) 201.

[68] CLEO collaboration Nucl. Inst. and Meth. **A379** (1992) 66.

[69] E. Aker et al, Nucl. Inst. and Meth. **A321** (1992) 69.

[70] V. Zhilich private communication.

[71] H. K. Jang private communication.

List of Figures

2.1 Results of C and P transformation on neutrino states. Only (a) and (d) are observed in neutrinos. 7
2.2 Weak transition of quarks. 8
2.3 Six unitarity triangles following from the orthogonality of the CKM matrix. 10
2.4 Feynman diagram of $B\bar{B}$ mixing. 11
2.5 Allowed region in the $\rho - \eta$ plane estimated from presently available data. Solid curves : $|V_{cb}|$, $|V_{ub}|/|V_{cb}|$, ϵ, Re(ϵ'/ϵ), x_d and m_t as constraints; Dashed curves : without x_d and Re(ϵ'/ϵ). The inner (outer) curves denote 1σ (90% C.L.) regions. 12
2.6 Feynman diagram for $B^0 \to J/\psi K_s^0$ 13
2.7 Measurement of time difference (t'-t) for $B^0 \to$ J/ψ K_s. 13
2.8 Feynman diagram for B tagging. 15
2.9 Proper time distribution of t'$-$t in $B \to J/\psi K_s^0$. 15
2.10 Feynman diagram for $B^0 \to K^+\pi^-$.(a)tree diagram and (b)penguin diagram. 16

3.1 Configuration of KEKB accelerator system. 18
3.2 BELLE detector. 20
3.3 Beam pipe. 23
3.4 Silicon vertex detector. 23
3.5 Central drift chamber. 24
3.6 Aerogel Čerenkov counters. (a)barrel (b)endcap. 26
3.7 Time of flight counter and trigger scintillator. 27
3.8 BELLE DAQ system 28
3.9 BELLE trigger scheme. 29

4.1 (a) Distribution of the opening angle of 2 γ's decaying from π^0 and (b)momentum dependence of the minimum opening angle. 31

4.2 Momentum spectrum of inclusive (a)γ's and (b)π^0's from B meson decays. 32

4.3 Energy spectrum of γ's in the process of (a) $B \to K^*\gamma$ and (b) $B \to \pi^0\pi^0$. 33

4.4 Energy spectrum of the e^+, e^- and γ from the Bhabha scattering. . . . 33

4.5 (a) Photon total attenuation as a function of energy in CsI. (b) Fractional energy loss of electrons and positrons per radiation length in lead as a function of energy. 34

4.6 Effect of electronics noise on the energy resolution by MC simulation. Energy is obtained by the sum of 5 × 5 CsI(Tℓ) counters 37

4.7 Overall design of the CsI(Tℓ) calorimeter. 40

4.8 Dimension of the barrel CsI(Tℓ) crystal. 42

4.9 (a)Layout of the forward endcap CsI(Tℓ) calorimeter and (b) expanded view of its 1/16. The crystal front face projected to a plane perpendicular to the beam is drawn. There are no gaps between crystals. 43

4.10 Expanded view of 1/16 of the backward endcap CsI(Tℓ) calorimeter. . 43

4.11 Dimensions of the endcap CsI(Tℓ) crystal. (1,2,3,4) or (1,2,3,4,5) is top plane and (5,6,7,8) or (6,7,8,9,10) is bottom plane. The top and bottom planes are in parallel. 44

4.12 (a)Setup of the ^{137}Cs source test, (b)the ADC distribution of reference crystal and (c)the typical ADC distribution of 9 subparts in a large crystal. 46

4.13 Results of ^{137}Cs source test. (a)average light output and (b)non-uniformity for sample counters. 47

4.14 Size measurement device for CsI(Tℓ) crystals. 48

4.15 Results of the size measurements for all the barrel crystals. Each histogram is the difference (in mm) between the specified size and the measured size. For definition of parameters, see Fig.**??**. 48

4.16 (a)Light output as a function of the dose for front-face irradiation. Upper: PMT-readout, Lower: PD-readout; The thick line represents the requirement for the radiation hardness of BELLE-ECL. (b)Position dependence of the light output measured by the PMT and PD readout. The data for front-face irradiation and uniform irradiation are shown; the circles, triangles, and squares stand for the data of 10, 100 and 1000 rad irradiation, respectively. All the values of the light output are normalized to those before irradiation. 49

4.17 Assembly of CsI(Tℓ) counter module. 51

4.18 Change of light output as a function of teflon thickness. 52

4.19 LED light output by changing the temperature with (a) epoxy (ECCOBOND 24) and (b) silicone rubber(KE109). The circles show the light output from photodiode with crystal. The squares show the photodiode and preamplifier results without crystal. In the case of KE109, the glue joint was broken around 31 degree and recovered after increasing the temperature to lower than the broken point. For the case with crystal, the temperature cycle is 27 °C → 50 °C → 27 °C → 0 °C → 20 °C. 53
4.20 Mechanical structure for holding the CsI(Tℓ) counters. (Left) Before and (Right) after attaching the compartment wall to the inner wall. . 54
4.21 Illustration of installed counters in the compartment. 55
4.22 (a) Change of light output with pressure applied on the crystal surface. (b) Uniformity of light output with pressure. 56
4.23 Block diagram of the CsI(Tℓ) readout electronics. 57
4.24 Schematics of the photodiode, preamplifier and shaper system. 58
4.25 Each parts of the preamplifier. 62
4.26 Preamplifier test setup for (a) test pulse (b) ^{241}Am source and (c) LED. 62
4.27 Results of the preamplifier test. 64
4.28 Operation of the three range of MQT300. 64
4.29 Signals supplied to the TDC. Two examples are given for MQT300 output to TDC; one for the pedestal and the other for the small pulse height. 65
4.30 (a)LED driving circuit in shaper/QT module, (b)the signal to trigger the driver and (c)the signal supplied to LED. 66
4.31 LED light output and the linearity for three ranges as a function of driving pulse height. 67
4.32 Shape of test pulse. 67
4.33 Block diagram of the CsI(Tℓ) trigger system. 68
4.34 Schematic diagram of STM module. 69
4.35 Calorimeter division for Bhabha event selection. 71
4.36 Segmentation for cosmic ray veto. 71

5.1 Cosmic ray stand. 74
5.2 (a)Definition of CsI(Tℓ) crystal subparts and (b)the distribution of TDC counts/cm in 9 subparts. 76
5.3 Examples of the uniformity of the light output for 9 subparts. The solid line is the fitting by the 3rd order polynomial. 77

5.4 (a)Most probable energy deposit of cosmic ray in CsI counter (GEANT simulation). (b)The differential intensity of the cosmic ray. 78

5.5 Energy deposit of cosmic rays in a photodiode (a)data and (b)GEANT simulation. 78

5.6 Results of the light output for all CsI(Tℓ) counters 79

5.7 Reproducibility of (a)the light output and (b)position dependence after 6 months. 80

5.8 (a)Comparison between the calibration by cosmic rays and the ^{137}Cs source. (b)Ratio between two calibrations. 80

5.9 Position Dependence of light output. (a-c): Measurement by photodiode glued on the crystal. (d-f): Measurement by phototube with air gap. (g-i): Difference between two methods. 82

5.10 Distribution of uniformity. 83

6.1 (a) Compton scattering and (b) Bremsstrahlung scattering. 85

6.2 Layout of the photon beam line. 85

6.3 Experimental setup – 1. CsI(Tℓ) counters; 2. drift tube hodoscopes; 3. plastic scintillation counters for cosmic trigger; 4. lead collimator; 5. veto counter; 6. movable platform for the position adjustment. 87

6.4 Beam test setup and crews. 88

6.5 6×6 CsI(Tℓ) matrix and crystal numbering (Front view). 89

6.6 Schematics of trigger and data acquisition for the beam test. 91

6.7 History of (a)pedestal and (b)it's width over 2 months. 92

6.8 Typical pedestal distribution of (a) one channel and (b) the sum of 36 channels after conversion to energy unit. 93

6.9 Test pulse calibration for (a) High, (b)Middle and (c)Low ranges. (d)-(f) shows the deviation from the linear fitting in % for each range. 94

6.10 Stability of the test pulse slope in (a) High, (b)Middle and (c)Low range of MQT. 95

6.11 Stability of the test pulse ratio for (a)H/M and (b)M/L for a typical channel. The stability is within 0.1 %. 96

6.12 Pulse height distribution for the back scattered Compton photons for 1 counter. The theoretical Compton edge is at 508 MeV. 97

6.13 Distribution of beam calibration constants for central 16 counters. . . 98

6.14 Ratio of the cosmic-ray calibration to the beam calibration. 99

6.15 Position dependence of the light output measured by cosmic rays for (a) all counters and (b) central four counters after scaling to the average light output of each counter. 99

6.16 Energy deposit in longitudinal slices of the CsI(Tℓ) crystal for 508 MeV Compton beam. The depth of each slice is 3 cm. 101

6.17 Temperature dependence of cosmic-ray calibration. Lines indicate the temperature at several locations in the data taking room, and stars are the average of the cosmic-ray calibrations of 36 counters. 102

6.18 (a)Correlation between the energies E_{CsI} and E_{tag} for 508 MeV Compton run. (b)Distribution of R_E with fitting . The fitting region is 410 $\sim$ 510 MeV. 103

6.19 Typical Compton edge distributions. The solid line in each figure is the fitting results. 104

6.20 Compton photon distribution with two photon background by Monte Carlo simulation. The percentage of 2 photon is 20 % of the single photon. 104

6.21 (a)Typical Bremsstrahlung distribution for 4036 MeV electron beam and (b)the expanded view of the edge region with fitting result. 105

6.22 Energy dependence of asymmetry parameter η obtained from the fitting of R_E for (a)5x5 and (b)3x3 matrix with fitting. 106

6.23 Energy resolution as a function of incident photon energy for (a)3 × 3 and (b) 5 × 5 matrix by the simple sum. The energy resolution of (c)3 × 3 and (d)5 × 5 matrix with the threshold of 0.5 MeV. Solid lines are results of the fitting. The resolution of the tagging system is given in seven separate lines below the data points. 107

6.24 Most probable number of counters with energy deposit greater than the threshold. 109

6.25 Number of counters used in the summation of energy vs energy resolution. 110

6.26 Threshold dependence of the energy resolution. 111

6.27 Position of beam injection point by the center of gravity method for (a)(c)1810.MeV (b)(d)5441.MeV. (a)(b) are data and (c)(d) are Monte Carlo simulation (MC) results. (e)(f) are the real beam injected points in MC. Left figures show X_c vs Y_c , middle figures show X_c distribution and right figures show Y_c distribution. The unit is the edge length of one crystal. 113

6.28 Comparison between data (cross) and simulation (histogram) of the R_E distribution for (a)27.5, (b)75, (c)300 and (d)500 MeV photon. The right figures are expanded view near the peak. 114
6.29 Comparison between real data (cross) and simulation(histogram) of the Compton edge of (a)29.4, (b)76.8, (c)291.5 and (d)508.3 MeV. The right figures are expanded view of the edge part. 115
6.30 Monte Carlo simulation (MC) results of energy resolution of (a)3×3 and (b)5×5 counters, and energy resolution of (c) 3×3 and (d) 5×5 with threshold = 0.5MeV. Tagging System resolution which are drawn by solid line is included in MC and subtracted after fitting. 116
6.31 Energy resolution of 5×5 matrix with threshold of 0.5 MeV. The solid line is the fitting to the Monte Carlo resolution (see Fig. **??**d). CLEO II beamtest results are obtained for 3×3 matrix. 117
6.32 R_E distribution with different fitting regions for $E_\gamma = 25$ MeV. Different fitting regions correspond to removing histogram bins less than 5, 10, 20 % of the peak bin. 118
6.33 (a)Correlation of the generated R_E resolution σ_{in} and obtained resolution σ_{out} after fitting and subtraction of the TS resolution with $\sigma_{TS} = 3.3\%$. (b)Results of the same practice for the Compton edge resolution. 119
6.34 (a)Incident photon beam energy vs measured energy in CsI for data. (b)Energy linearity for data. 121
6.35 Energy linearity for MC. 122
6.36 Energy linearity for Monte Carlo simulation. Perfectly uniform light output is assumed. 122
6.37 Difference of energy linearity between data and M.C. 123
6.38 Time dependent correction factor determined by cosmic calibration. The reference point is the cosmic data nearest to the beam calibration run, which is not included in this plot. 124
6.39 Variation of fitted Compton edge with different amount of 2 photon background simulation study. 124
6.40 Electronics linearity measured by the test pulse for $0 - 100$ MeV. . . . 126
6.41 (a)Setup of the linearity measurement by using the ^{137}Cs and ^{60}Co sources and the spectrum with (b)photomultiplier and (c)photodiodes. (d)Correlation between photomultiplier data and photodiode data. (e)Photodiode spectrum corresponding to 662 keV ^{137}Cs photopeak selected by the photomultiplier data. 128

6.42 (a)Energy linearity measured by using the ^{137}Cs and ^{60}Co and (b)deviation from the linear response. 129

7.1 First interaction points of 100 MeV γ's generated uniformity in the detector. 132

7.2 (a)Opening angle between CsI cluster and the generated γ and (b) Polar angle dependence of the average opening angle. 133

7.3 (a)E_9/E_{25} distribution after 'cut 1' (opening angle $\leq 2.5°$), and (b)R_γ distribution after 'cut 2' ($E_9/E_{25} \geq 0.9$). 134

7.4 Momentum dependence of γ detection efficiency for (a)inner detector ON and (b)OFF after applying all selection cuts. 134

7.5 Polar angle (θ) dependence of γ detection efficiency. 135

7.6 Invariant mass $M_{\gamma\gamma}$ distribution of any combination of 2 γ clusters for each momentum region ($0-0.1$, $0.1-0.2$, $0.2-0.3$, $0.3-0.5$, $0.5-1.0$, $1.0-2.0$ GeV), for $B\bar{B}$ generic events. The number of generated events is 25,000. 136

7.7 π^0 momentum distribution (reconstructed momentum/generated momentum) for all momentum regions with logarithmic Gaussian fit. . . . 137

7.8 Momentum dependence of π^0 detection efficiency after each cut. (cut1 : opening angle between generated γ and the reconstructed cluster $\leq 2.5°$ for 2 γ's, cut2 : $E_9/E_{25} \geq 0.9$. for 2 γ's, cut3 : $M_{\pi^0} - 3\sigma_{M_{\pi^0}} \leq M_{\gamma\gamma} \leq M_{\pi^0} + 3\sigma_{M_{\pi^0}}$, cut4 : $\hat{R}_{\pi^0} - 3\sigma^L_{R_{\pi^0}} \leq R_{\pi^0} \leq \hat{R}_{\pi^0} + 3\sigma^H_{R_{\pi^0}}$.) 138

7.9 Momentum dependence of π^0 detection efficiency for (a)inner detector OFF and (b)ON. The efficiency is shown for Barrel and Forward, Backward endcap calorimeter separately. 139

8.1 Installation of the BELLE calorimeter. 142

8.2 The first cosmic ray event seen after installation of the CsI(Tℓ) calorimeter into the BELLE detector (Oct. 1998) 144

8.3 The first cosmic ray event seen after installation of the CsI(Tℓ) calorimeter into the BELLE detector (Oct. 1998) 145

8.4 Distribution of the noise level for all the barrel counters after installation.146

A.1 Ingots of CsI(Tℓ) crystals produce by (a) Institute for Single Crystals in Ukraine and (b)Shanghai Institute of Ceramics. The Chinese crystals are grown by the Bridgman method. The Ukrainian crystals are produced by the Czochralski method. The growth speed of the crystal is $\sim$ 1 mm/hour in either method. 148
A.2 Crystal delivery for BARREL. 152

List of Tables

2.1 C, P, T transformation of physical observables. 6
2.2 Decay modes of B meson useful for the determination of unitarity triangle. 14

3.1 Parameters of KEKB accelerator. 19
3.2 Performance parameters of the BELLE detector 22

4.1 Resolution of typical electromagnetic calorimeters. E is in GeV. 36
4.2 Properties of several inorganic crystal scintillators. 41
4.3 The geometrical parameters of the CsI Calorimeter. 42
4.4 Specifications of photodiode. 60
4.5 Results of the preamplifier performance measurements. 63
4.6 Conditions to trigger Bhabha events. The numbers are (2+11+3)-fold ϕ-ring sums depending on θ direction. 70

6.1 Summary of the beam setup in the beam test. 90
6.2 Systematic error estimation of (a)Compton photon and (b)Bremsstrahlung photon(unit : %). 125

7.1 Cut dependence of the γ detection efficiency for $B\bar{B}$ events. Detector geometrical acceptance is included in the efficiency. 135
7.2 π^0 detection performance of BELLE CsI(Tℓ) calorimeter for (a) Inner detector ON and (b) OFF. 140

B.1 Barrel crystal size 1. 153
B.2 Barrel crystal size 2. 154
B.3 Barrel crystal size 3. 154
B.4 Barrel crystal size 4. 155
B.5 Forward endcap crystal size 1. 156
B.6 Forward endcap crystal size 2. 157
B.7 Forward endcap crystal size 3. 158

B.8 Forward endcap crystal size 4. 159
B.9 Forward endcap crystal size 5. 160
B.10 Backward endcap crystal size 1. 161
B.11 Backward endcap crystal size 2. 162
B.12 Backward endcap crystal size 3. 163
B.13 Backward endcap crystal size 4. 164